

1 Understanding hydrologic controls of slope-sloping soil 2 response to precipitations through Machine Learning 3 analysis applied to synthetic data

4 Daniel Camilo Roman Quintero¹, Pasquale Marino¹, Giovanni
5 Francesco Santonastaso¹, Roberto Greco¹

6 ¹Dipartimento di ingegneria, Università degli Studi della Campania 'Luigi Vanvitelli',
7 via Roma 9, 81031 Aversa (CE), Italy;

8 *Correspondence to:* Daniel Camilo Roman Quintero
9 (danielcamilo.romanquintero@unicampania.it)

10 **Abstract:**

11 ~~The assessment of the response of slopes to precipitation is important for various~~
12 ~~applications, from water supply management to hazard assessment due to~~
13 ~~extreme rainfall events. It is well known that the~~Soil and underground conditions
14 prior to the initiation of rainfall events control the hydrological processes that
15 occur in slopes, affecting the water exchange through their boundaries. The
16 present study aims at identifying suitable variables to be monitored ~~and modelled~~
17 to predict the response of ~~the slope-sloping soil~~ to precipitations. ~~A~~The case ~~study~~
18 ~~consisting~~ of a ~~loose~~ pyroclastic coarse-grained soil ~~cover~~mantle overlaying a
19 karstic bedrock ~~located~~ in the ~~southern~~Southern Apennines (Italy) is described,
20 ~~where field~~Field monitoring ~~has been carried out, comprising of~~ stream level
21 recordings, meteorological ~~recordings~~variables, and soil water content ~~and~~
22 ~~suction~~ has been carried out for few years among others. Nevertheless, tTo
23 ~~enhance~~enrich the field dataset, a synthetic series of 1000 years has been
24 ~~generated~~the slope hydraulic behaviour of the case study has been simulated with
25 a physically based model ~~linked~~coupled to a ~~synthetic~~stochastic rainfall ~~time~~
26 ~~series~~model, ~~getting a consistent hourly timeseries dataset of 1000 years,~~
27 ~~containing information on rainfall, aquifer water level and soil volumetric water~~

28 ~~content at different depths~~. Machine Learning techniques have been used to
29 unwrap the non-linear cause-effect relationships ~~amongst linking the studied~~
30 ~~variables, which relations are commonly non-linear~~. The k-means clustering
31 technique has been used for the identification of seasonally recurrent slope
32 conditions, in terms of soil moisture and groundwater level, and the Random
33 Forest technique has been used to assess how the ~~way the slope response could~~
34 ~~be addressed and the importance of each variable conditions at the onset of~~
35 rainfall controlled on the slope response and attitude of the soil mantle to retain
36 much of the infiltrating rainwater~~the k-means clustering technique has been used~~
37 ~~to explore the geometrical disposition of data, and so the identification of~~
38 ~~seasonally recurrent different scenarios linked to the slope response~~. It has been
39 The results shown that the ~~slope~~ response in terms of the fraction of rainwater
40 being remaining stored in the soil mantle at the end of rainfall events~~cover~~ is
41 naturally highly dependent on the rainfall amount, but water drainage and storage
42 processes can be identified by normalizing the change in water storage with the
43 rainfall depth. Indeed, with the methodology presented here, different
44 hydrometeorological scenarios controlling major hydrological processes have
45 been identified not only from the meteorological and seasonal behaviour but also
46 from the underground conditions controlled by soil moisture and groundwater
47 level prior to the rainfall initiation, ~~weighting the role, on one hand, of the field~~
48 ~~capacity value on the ease of the water to flow in and out of the soil cover and,~~
49 ~~on the other hand, of the ground water level, the increase of which gives~~
50 evidence of the activation of slope-effective drainage processes~~even during~~
51 relatively intense rainfall events.

52 **Keywords:** Water storage, slope response, underground antecedent conditions,
53 hydrological controls, Random Forest, k-means clustering

54 **1. Introduction**

55 Slope response to precipitations is highly non-linear, in terms of runoff
56 generation, rainwater infiltration and subsurface drainage processes, which are
57 mostly depending on the initial soil moisture state at the onset of ~~the each~~ rainfall
58 event (Tromp-Van Meerveld and McDonnell, 2006b; Nieber and Sidle, 2010;
59 Damiano et al., 2017). The initial (or antecedent) conditions are related to
60 hydrological processes that occur in the slopes, which control ~~water-how they~~
61 exchanges ~~between the slope and water with the~~ surrounding systems (i.e.,
62 atmosphere, surface water, deep groundwater). These processes occur through
63 the boundaries of the slope, and often evolve over ~~long~~-timescales of weeks or
64 even months, much longer than the duration of rainfall events, typically ranging
65 between some hours and few days.

66 While the importance of ~~antecedent-soil moisture~~ conditions on ~~overland-slope~~
67 runoff and drainage has been ~~early identified, and their role as predisposing~~
68 ~~conditions has already been recognized~~ recognized long since (Ponce ~~and~~
69 Hawkins, 1996; Tromp-Van Meerveld ~~&and~~ McDonnell, 2006a, 2006b), only
70 recently the scientific community started providing new perspectives to better
71 understand ~~slope-predisposing-hydrologic~~ conditions predisposing slopes to
72 landslides (Bogaard and Greco, 2018; Greco et al., 2023), to explain why most
73 of large rain events do not destabilize slopes, while only some do (Bogaard and
74 Greco, 2016), and ~~so to develop~~ physically-based models capable of integrating
75 ~~this~~ hydrological knowledge for predicting ~~their-landslide~~ occurrence have been
76 proposed (e.g., Bordoni et al., 2015; Greco et al., 2018; Marino et al., 2021;
77 Bordoni et al., 2015).

78 The triggering of some rainfall-induced geohazards, such as shallow landslides
79 and debris flows, is favoured by pore pressure increase, caused by rainwater
80 infiltration and consequent soil moisture accumulation. The storage of ~~infiltrating~~
81 rainwater within the soil ~~also~~ requires drainage mechanisms developing in the

82 slopes in response to precipitations to be not so effective to drain out much of the
83 infiltrating rainwater (Marino et al., 2020b; Greco et al., 2021; 2023).
84 Consequently, especially for nowcasting and early warning purposes, the
85 identification of hydrological variables suitable to identify slope predisposing
86 conditions is extremely useful. Thus, to better understand how ~~the complex~~
87 hydrological predisposing conditions may control the processes involving the
88 slope-sloping soil response in terms of water storage, a field monitoring ~~campaign~~
89 allowing for the assessment of the slope water balance is highly recommended
90 (Bogaard and Greco, 2018; Marino et al., 2020a).

91 The identification of suitable variables to be monitored in the field is indeed
92 useful to achieve an insight of the behaviour of the interconnected hydrological
93 systems (i.e., groundwater, surface water, soil water). Besides the study
94 of rainfall-induced landslides, The the proper evaluation of the hydrological
95 scenarios in a region of interest could impact several other applications, from
96 flood hazard assessment ~~and the study of rainfall induced landslides~~ (Bogaard
97 ~~and Greco 2016~~ Reichenbach et al., 1998; Forestieri et al., 2016; Chitu et al.,
98 2017), to the prediction of possible crop water stress conditions in relation to
99 defoliation (Capretti and Battisti, 2007), pathogen expansions in chestnut grove
100 (Gao and Shain, 1995), and plant mortality in a climate change context ~~as well~~
101 (McDowell et al., 2008).

102 This research focuses on a case study of a slope located in Campania (southern
103 Italy), in an area ~~sensitive to problems associated to both dry and wet seasons,~~
104 ~~but where particularly frequently hit by~~ destructive ~~rainfall-rainfall-triggered~~
105 shallow landslides ~~occurred~~. Such geohazards are recurrent along the carbonate
106 slopes covered with unsaturated pyroclastic deposits typical of the area (Fiorillo
107 et al., 2001; Revellino et al., 2013). The underlying limestone bedrock, densely
108 fractured, is characterised by the presence of deep karst aquifers (Allocca et al.,
109 2014). The triggering of rainfall-induced shallow-mechanism of landslides in the

110 ~~area is controlled by~~ the increase of water storage within the soil ~~cover~~-mantle
111 after intense and persistent precipitations, leading to pore pressure build up
112 (Bogaard and Greco 2016). ~~Such geo hazards are recurrent along the slopes~~
113 ~~covered with unsaturated pyroclastic deposits typical of wide areas of Campania,~~
114 ~~southern Italy (Fiorillo et al., 2001; Revellino et al., 2013).~~ Slope equilibrium is
115 in fact guaranteed by the additional shear strength promoted by soil suction (Lu
116 and Likos 2006; Greco and Gargano 2015), which reduction often leads to slope
117 failure due to shear strength loss by soil wetting during rainwater infiltration
118 (Olivares and Picarelli, 2003; Damiano and Olivares, 2010; Pagano et al., 2010;
119 Pirone et al., 2015).

120 ~~Not only the rainfall characteristics and the soil saturation play a role in the~~
121 ~~hydrological slope response to precipitations.~~ Recent studies show that the
122 response of the soil covers mantle to precipitations in the study area is affected
123 not only by rainfall characteristics and antecedent soil moisture, but also by the
124 wetness of the ~~soil bedrock~~-interface with the underlying bedrock, which controls
125 the leakage of water into the underlying fractured limestone (Marino et al.,
126 2020a; ~~b~~ 2021). At the contact between soil ~~cover~~ and bedrock, intense
127 weathering modifies the physical properties of the soil as well as of the fractured
128 bedrock, which ~~seem to be form a~~ hydraulically interconnected system, the
129 epikarst (e.g., Perrin et al., 2003; Hartmann et al., 2014; Dal Soglio et al., 2020).
130 The changing hydraulic behaviour of the soil-bedrock interface can be related to
131 the storage of water in the epikarst, where a perched aquifer forms during the
132 rainy season uppermost part of the fractured bedrock (Greco et al., 2014, ~~2014~~
133 2014). ~~Therefore, the aquifer water level arises as another possible monitoring~~
134 ~~variable to be considered within slope controls.~~

135 The aim of this study is to identify the major hydrological processes controlling
136 the ~~slope~~-response of the slope soil mantle to precipitations, and the seasonally
137 recurrent conditions that affect its attitude to retain much of the infiltrating

138 ~~rainwater, the most suitable through suitable measurable variables to quantify~~
139 ~~them. To this aim, a rich dataset of measured rainfall events and corresponding~~
140 ~~hydrological effects would be required, which was not available for the case~~
141 ~~study, where monitoring activities had been carried out for few years. Therefore,~~
142 ~~a synthetic 1000 years hourly dataset was generated, by means of a stochastic~~
143 ~~rainfall model and a simplified methodological approach gathering wide~~
144 ~~knowledge on field process simulations and data analysis is presented. In that~~
145 ~~way, a 1-D physically based mathematical model of the slope, that couples~~
146 ~~coupling the interaction between the unsaturated pyroclastic soil cover mantle~~
147 ~~and the underlying perched aquifer (Greco et al., 2018), was applied to describe~~
148 ~~the behaviour of a slope located in Campania (southern Italy), under a 1000 years~~
149 ~~long hourly rainfall synthetic time series. The Both models had been previously~~
150 ~~calibrated and validated on field experimental data from field monitoring carried~~
151 ~~out since 2001 (Damiano et al., 2012; Greco et al., 2013; Comegna et al., 2016;~~
152 ~~Marino et al., 2021 Damiano et al., 2012). The results of the simulations provide~~
153 ~~the synthetic time series data of soil suction, water content and aquifer water level,~~
154 ~~all measurable in the field and assumed as representative of real field conditions,~~
155 ~~were analysed as if they were measured data. Once After identified sorting the~~
156 ~~rainfall events within the 1000-years hourly timeseries, a specific dataset is was~~
157 ~~built with the antecedent conditions one hour before the beginning of any each~~
158 ~~rainfall event, comprising It included the previously named listed variables plus~~
159 ~~the total event rainfall amount depth, and the change in the water stored in the~~
160 ~~soil cover mantle at the end of the each rainfall events. To disentangle the non-~~
161 ~~linear processes controlling the hydraulic behaviour of the slope, and their role~~
162 ~~on the soil response to precipitation, the dataset was analysed with Machine~~
163 ~~Learning (ML) techniques, i.e., clustering, and random forest. Indeed, ML~~
164 ~~allows managing big amounts of data, such as those provided by assimilation of~~
165 ~~extensive monitoring networks, remote sensing, satellite products and other~~
166 ~~sources, without introducing any mathematical model structure to highlight the~~

167 cause-effect relationships linking the variables. ~~to disentangle the nonlinear~~
168 ~~processes controlling the slope hydraulic behaviour due to rainfall events, and~~
169 ~~thus to identify the role played by the variables, suitable to be monitored in the~~
170 ~~field, on the slope response to precipitations.~~

171

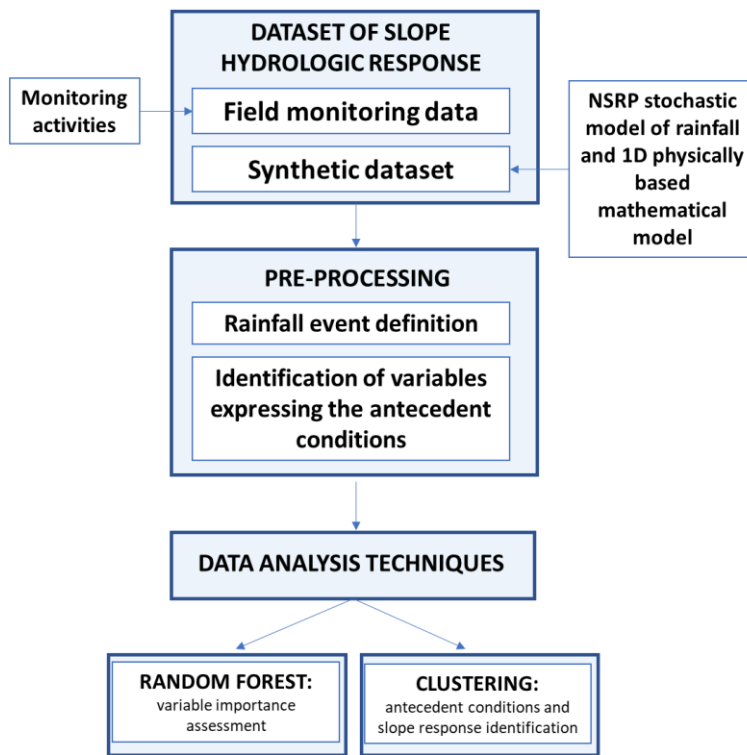
2. Materials and methods

The studied slope, described in section 2.1, belongs to the Partenio Massif, and it has the typical characteristics of many pyroclastic slopes of Campania (southern Italy) (Greco et al., 2018). Indeed, three major zones characterized by unsaturated pyroclastic deposits can be identified in Campania (Cascini et al., 2008): Campanian Apennine chain, composed by carbonate rock covered by a variable layer of pyroclastic soil (from 0.1 to 5 m); Phlegraean district, formed by underlying densely fractured volcanic tuff bedrock, placed under several meters of pyroclastic soils; and Sarno and Picentini Mountains, where a thin layer of pyroclastic material is over a terrigenous bedrock. In these three areas, the thickness of the soil ~~covers mantle results is~~ quite variable, according to the slope inclination and to the distance from the eruptive centre (De Vita et al., 2006; Tufano et al., 2021).

To identify the seasonally recurrent conditions that affect the attitude of the soil mantle to retain much of the infiltrating water, a large set of measurements of rainfall events, and their effects on the slope, would be required. Hence, to enrich the data available from the monitoring activities carried out for some years at the slope (Marino et al., 2020a), A synthetic dataset of ~~slope the~~ hydrologic response of the slope to precipitations, has been generated with a NSRP stochastic model of rainfall (Rodriguez-Iturbe et al., 1987) and a simplified 1D model of ~~based on soil cover the~~ interaction of the unsaturated pyroclastic soil mantle with rainfall (in the uppermost boundary) and the underlying shallow perched aquifer (in the lowermost boundary), has been built forming in the epikarst. Both the models, described in the following sections, had been previously developed based on experimental data (Greco et al., 2013; 2018; Marino et al., 2021). The obtained synthetic dataset has been compared to the limited dataset from field monitoring, showing a reasonable agreement. Therefore, it has been considered ~~reliable suitable~~ to reproduce slope response to

200 climate forcing, in terms of soil volumetric water content, and perched aquifer
201 water level, in the studied area (see Section 2.2) and rainfall.

202 ~~Moreover, the~~ obtained synthetic data-set has been analysed with Machine
203 Learning techniques (Section 2.3), as they result quite powerful to identify non-
204 linear cause-effect relationships between variables, without introducing any
205 model structure, as if the data were provided by field measurements. ~~Besides, the~~
206 ~~results which come from these data analyses have been compared a priori to the~~
207 ~~limited dataset from field monitoring, showing a reasonable agreement.~~ Figure 1
208 shows the flowchart of the entire methodology.

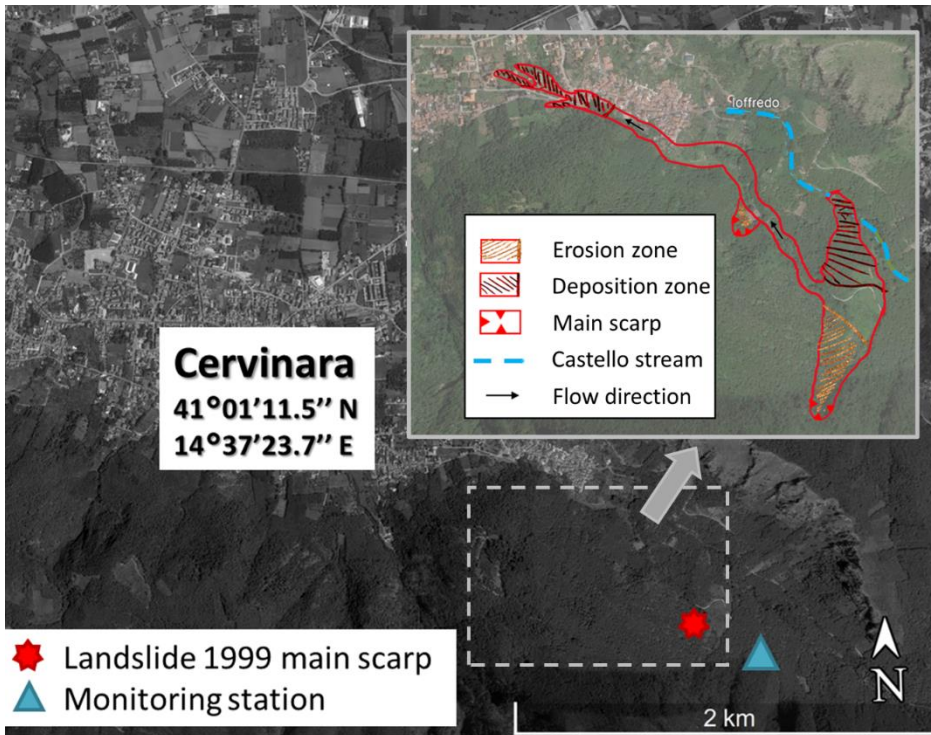


209
210 Figure 1. Flowchart summarizing the methodology followed in the analysis
211 of sloping soil response to precipitation.

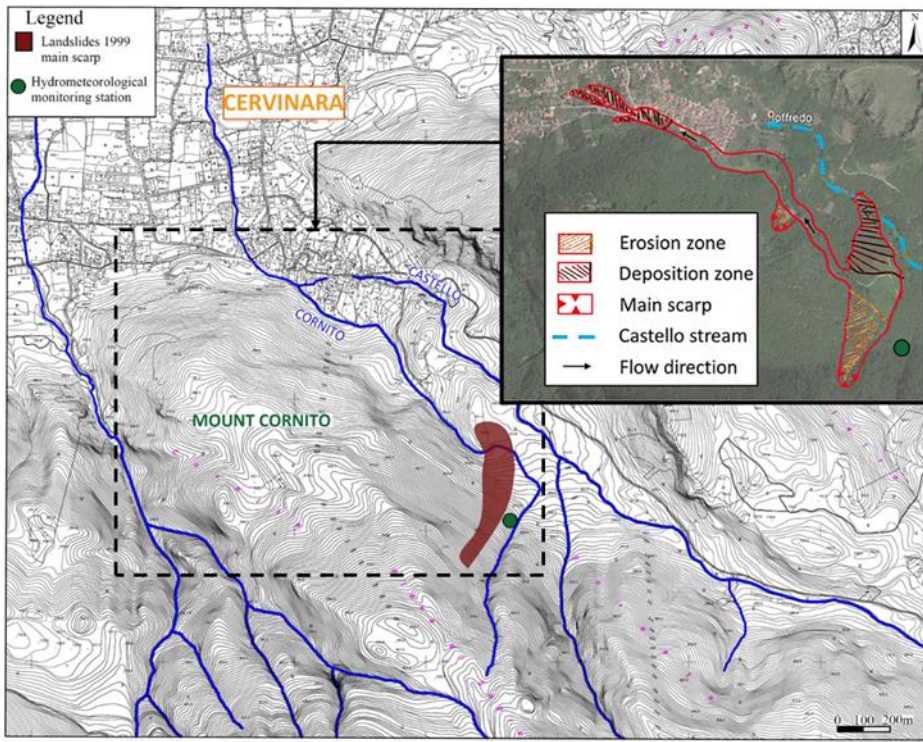
212 **2.1. Case study**

213 The study area refers to the north-east slope of Monte Cornito, part of the Partenio
214 Massif (Campania, southern Italy), 2 km from the town of Cervinara, about 40
215 km northeast of the city of Naples. The slope was involved in a series of rapid
216 shallow landslides after a rainfall event of 325 mm in 48 hours during the night
217 between 15–16 December 1999, causing casualties and heavy damages (Fiorillo
218 et al., 2001). A field monitoring station was installed nearby the big landslide
219 scarp since 2001. Further details of the investigated zone, with indications of the
220 area affected by the largest of the landslides triggered in 1999, are shown in

221 Figure 2~~Figure 1~~.



222



223

224 **Figure 21. Location of the study area and indication of the zone affected by a large**
225 **landslide in 1999[†]**

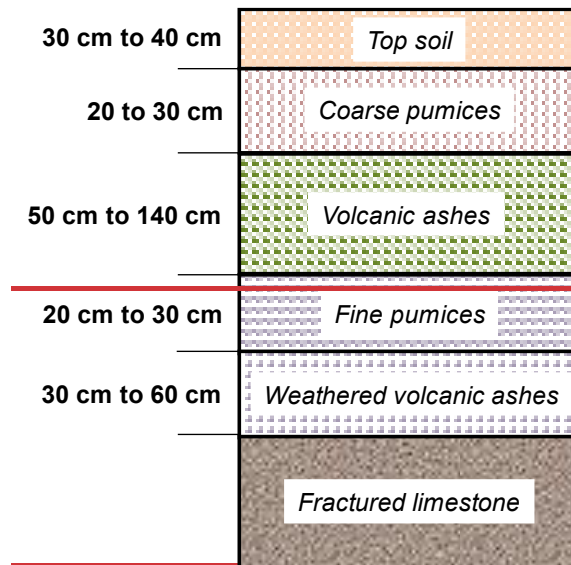
226 Partenio Massif is part of the southern Apennines area. The bedrock mainly
227 consists of Mesozoic-Cenozoic fractured limestones, mantled by loose
228 pyroclastic deposits, resulting from the explosive volcanic activity of Somma-
229 Vesuvius and Phlegrean Fields, which occurred over the last 40.000 years
230 (Rolandi et al., 2003).

231 The fractured limestone formations of the southern Apennines often host large
232 karst aquifers, through which a basal groundwater circulation occurs, for which
233 regional groundwater recharge between 100 and 500 mm/year has been
234 estimated, with 200 mm/year regarding the area of Cervinara (Allocca et al.,
235 2014). Moreover, recent studies showed that, in the upper part of the karst system,
236 denoted as epikarst (Hartmann et al., 2014), more permeable and porous than the
237 underlying rock, a perched aquifer often develops (Williams, 2008; Celico et al.,
238 2010). It temporally stores water and favors the recharge of the deep aquifer
239 through the larger fracture system. The water, which is accumulated temporally
240 in the epikarst, also reappears at the surface in small ephemeral streams.

241 Specifically, the slope of Cervinara has an inclination between 35° and 50°, at an
242 elevation between 500 m and 1200 m above sea level. The soil ~~cover~~overmantle,
243 usually in unsaturated conditions, is the result of the air-fall deposition of the
244 materials from several eruptions, so it is generally layered. It mainly consists of
245 layers of volcanic ashes (with particle size in the range of sands to loamy sands)
246 alternating with pumices (sandy gravels), laying upon the densely fractured
247 limestone bedrock. Near the soil-bedrock interface, a layer of weathered ashes,

[†]Google (2022) *Cervinara, Italy*. Available at:
<https://www.google.com/maps/@41.0114559,14.6411297,2097m/data=!3m1!1e3> (Accessed: 7
March 2022)

248 characterized by finer texture (silty sand), with lower hydraulic conductivity,
249 moderate plasticity and low cohesion, is often observed (Damiano et al., 2012).



250

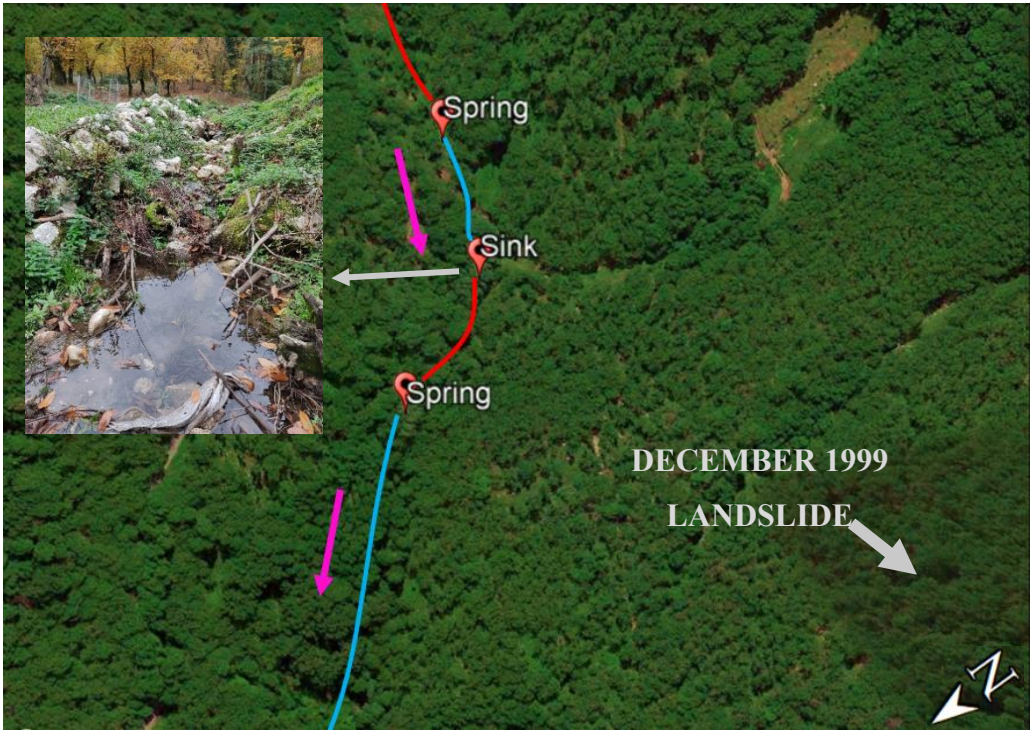
251 **Figure 2. Characteristic soil profile for the slope near the scarp of the landslide**
252 **occurred in 1999 in Cervinara**

253 The soil cover-mantle thickness varies spatially from a minimum of 1.0 m, in the
254 steepest part of the slope, to larger values at its foot (up to 4-5 meters). The thin
255 soil mantle, compared to the slope width and length of hundreds of meters (Figure
256 2), makes the flow processes nearly one-dimensional, except for the close
257 proximity to geometric singularities. Figure 2 shows the soil layers constituting
258 the cover, as found throughout the slope near the main scarp of 1999 landslide.

259 The pyroclastic ashes-soils of the profile usually exhibit are characterized by high
260 porosity (from about 50% for the pumices, up to 75% for the ashes) and quite high
261 values of saturated hydraulic conductivity (ranging up to the order of 4×10^{-5} m/s).
262 Thus, this kind of soil lets rainwater infiltrate even during the most intense
263 rainfall events, with little runoff generation, and it can store a large amount of
264 water: without approaching saturation. The values of soil capillary potential,
265 measured during the rainy season, rarely exceed -0.5 m, as observed also in other

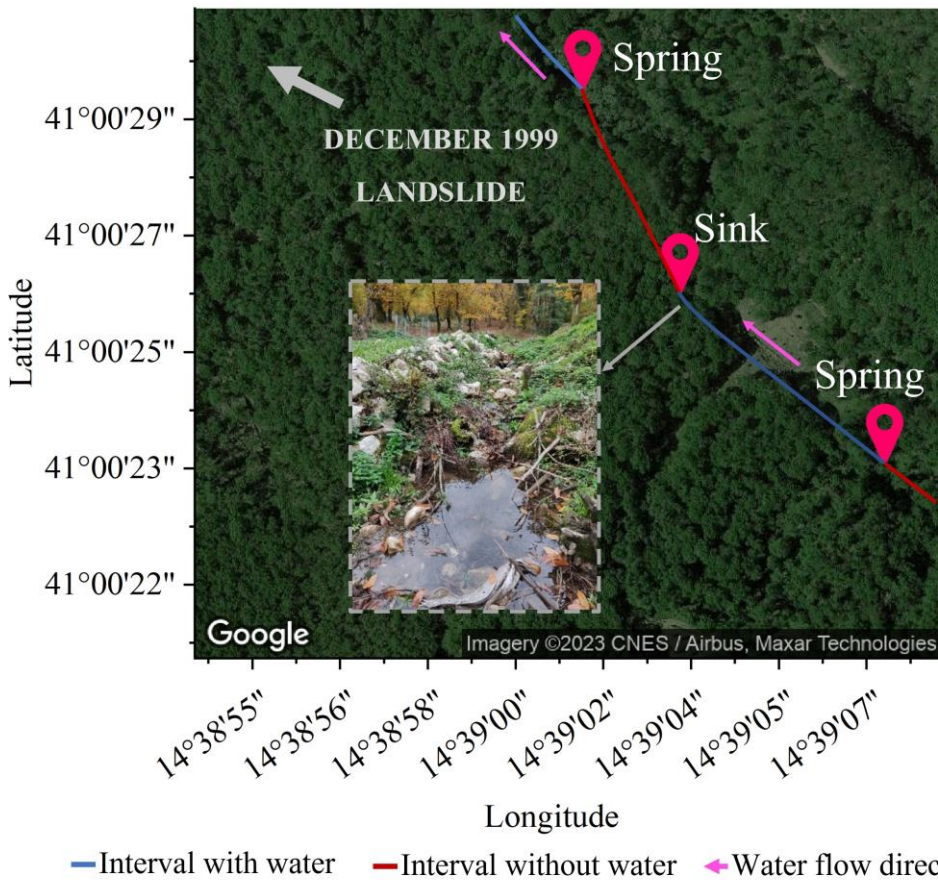
266 slopes of the area (Cascini et al., 2014; Comegna et al., 2016; Napolitano et al.,
267 2016).

268 The climate is Mediterranean, which is characterized by dry and warm summer
269 and rainy autumn and winter, with mean annual precipitation of about 1600 mm,
270 mostly occurring between October and April. The total potential
271 evapotranspiration ET_0 , estimated with the Thornthwaite formula (Shuttleworth,
272 1993), is between 700 mm and 800 mm in the altitude range between 750 m and
273 400 m (Greco et al., 2018). The vegetation mainly consists of widespread
274 deciduous chestnuts, with a dense understory of brushes and ferns, growing
275 during the flourishing period (between May and September). In fact, visual
276 inspections of the soil profile showed a large amount of organic matter and roots.
277 In most cases, roots are denser in the uppermost part of the soil ~~cover~~-mantle and
278 become sparse between the depth of 1.50 m and 2.00 m below the ground surface,
279 reaching the basal limestones and penetrating the fractures.



*Maps Data: Google, ©2022 CNES/Airbus, Maxar Technologies

— Interval with water — Interval without water ➔ Water flow direction



281
 282 **Figure 3. Identification of surface water flow in the Castello stream at the beginning**
 283 **of the rainy season in November 2021 by visual recognition of springs and sinks in**
 284 **the watercourse²**

285 Moreover, in the surrounding area, several ephemeral and perennial springs are
 286 present, mostly located at the foot of the slopes, which supply a network of small
 287 creeks and streams, allowing to show the activity of the aquifer discharge to the
 288 surface water. An indication regarding the Castello stream (the main stream for
 289 this side of the basin), with springs, is shown in Figure 3 ~~Figure 3~~, where, during
 290 a field recognition in November ~~the~~ 11th 2021, the surface water flow appeared
 291 (springs) and disappeared (sinks) in some points along the stream course.

² Google (2022) Cervinara, Italy. Available at:
<https://www.google.com/maps/@41.0088511,14.65137786m/data=!3m1!1e3> (Accessed: 7
 March 2022)

292 Normally the stream exhibits its lowest water depth values up to the beginning
293 of the late autumn (Marino et al., 2020a, p.3.3), but it is interesting to note that
294 the surface water in the stream emerging from the epikarstic springs is ~~feasible~~
295 ~~to be monitored as~~ an indicator of the active slope drainage ~~status~~.

296 **2.1.1. Field monitoring data**

297 Several hydrological monitoring activities have been carried out at the slope of
298 Cervinara since 2001, initially consisting of measurements of precipitations and
299 manual readings (every two weeks) of soil suction by “Jet-fill” tensiometers,
300 equipped with a Bourdon manometer (Damiano et al., 2012). Afterwards, since
301 November 2009, an automatic monitoring station has been set at an elevation of
302 585 m a.s.l., near a narrow track close to the landslide scarp of December 1999.
303 The installed instrumentation consisted of tensiometers, time domain
304 reflectometry (TDR) probes for water content measurements, and a rain gauge
305 (Greco et al., 2013; Comegna et al., 2016).

306 Since 2017, the hydro-meteorological monitoring was enriched (Marino et al.,
307 2020a), aiming at understanding the seasonal behaviour of the slope and the
308 interactions between the hydrological systems, i.e., the unsaturated soil
309 ~~cover~~mantle, the epikarst, and the underlying fractured bedrock.

310 Specifically, the data collected by tensiometers and TDR probes were
311 supplemented with those from a meteorological station (composed by a thermo-
312 hygrometer, a pyranometer, an anemometer, a thermocouple for soil temperature
313 measurement, and a rain gauge), and with the water level in two streams at slope
314 foot, so to gain useful information for the assessment of the water balance of the
315 studied slope.

316 The data ~~collected during these from~~ field monitoring ~~activities, carried out~~
317 between 2017 and 2020 with hourly resolution, consist of rainfall,
318 evapotranspiration, soil moisture and suction at various depths, and the water

319 depth of the Castello stream. The data have been useful to highlight seasonally
320 recurrent soil moisture distributions. More details about the measured data and
321 the observed recurrent seasonal behaviour ~~related to the moisture conditions of~~
322 ~~the soil profile~~ of the area of Cervinara can be found in Marino et al. (2020a).

323 2.2. Synthetic dataset

324 Aiming at identifying suitable variables to be monitored in the field for the
325 identification of the conditions controlling different slope responses to the
326 precipitations, a rich dataset of rainfall and underground monitored variables,
327 such as soil moisture and groundwater level, is needed. However, a complete
328 field monitored dataset is not always possible to be analyzed and, when it exists,
329 it is commonly available for short periods, granting a relatively low measurement
330 density. Hence, a synthetic dataset, aiming at improving the information obtained
331 from field monitoring, has been generated. This dataset has been obtained by
332 means of the physically based mathematical model described hereinafter (section
333 2.2.2). The model has been run with a 1000-years synthetic hourly rainfall series,
334 obtained with a stochastic rainfall generator, for which further details are given
335 in section 2.2.1.

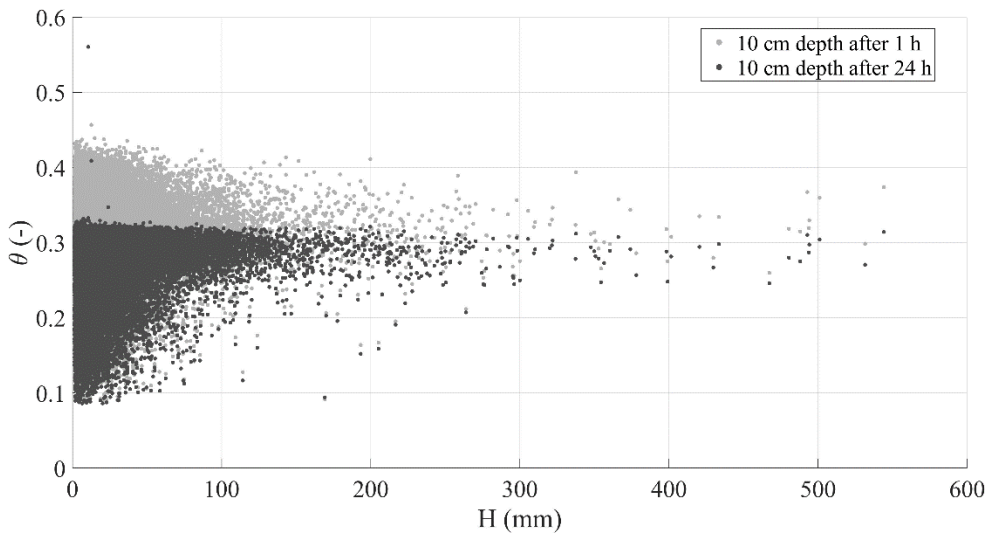
336 2.2.1. Definition of synthetic rainfall events

337 The Neyman-Scott rectangular pulse model (NSRP) has been used to obtain a
338 1000-years long synthetic hourly series of precipitations. The NSRP model
339 reproduces the precipitation process as a set of rain clusters, composed by
340 possibly overlapping rain cells embodied by rectangular pulses, each one with
341 random origin. The storm duration is represented by the cell width and its height
342 represents the associated rainfall intensity, so that when multiple cells overlap,
343 the total intensity is the sum of the intensities of the overlapping cells (Rodriguez-
344 Iturbe et al. 1987; Cowpertwait et al. 1996).

345 NSRP model calibration requires the identification of five parameters, using the
346 method of moments (Peres and Cancelliere, 2014), based on available rainfall
347 data for the investigated site. Specifically, the data from the rain gauge station of
348 Cervinara, situated near the Loffredo village, belonging to the Civil Protection
349 Agency of Campania Region available from January 2001 to December 2017
350 with a time resolution of 10 min, were used.

351 The aim of this study is the identification of variables expressing the slope
352 conditions responsible of different responses to precipitations. In that sense, it is
353 important to define the events within the rainfall time series to clearly distinguish
354 antecedent conditions from the effects of the current rainfall event.

355 In other words, within the 1000-years long time series, a criterion should be
356 identified to separate rainfall events, so that a new event begins only when the
357 effects of the previous one disappeared. For this study, the events were defined
358 as periods with at least 2mm of rainfall, preceded and followed by at least 24h
359 with less than 2mm (i.e., smaller than the mean daily potential evapotranspiration
360 estimated for the case study). Indeed, the separation period of 24 hours is
361 commonly used for the definition of the empirical thresholds for early warning
362 systems against rainfall-induced landslides (e.g., Peres et al., 2018; Segoni et al.,
363 2018, Marino et al., 2020b).



364

365 **Figure 4. Scatter plot of event rainfall depth and mean volumetric water content of**
 366 **the top 10 cm soil depth 1 hour (grey dots) and 24 hours (black dots) after the end**
 367 **of each rainfall event**

368 In fact, the mean volumetric water content (θ) at 10 cm depth below soil
 369 field capacity ($\theta \cong 0.35$) 24 hours after the end of each event (Figure 4) ~~Figure 4~~
 370 in all the cases in which such value was overcome ~~at~~ before the end of the event.
 371 This shows that a dry interval of 24 hours after a rainfall event is long enough for
 372 drainage processes to remove from the topsoil most of the water infiltrated from
 373 the previous event. As topsoil moisture controls the infiltration capacity at ground
 374 surface, after such interval the infiltration of new rainfall is only little affected by
 375 the remnants of the previous rainfall event.

376 With the assumed separation criterion, a total of 53061 rainfall events within
 377 1000 years are obtained, with durations ranging between 1 and 570 hours, and
 378 total rainfall depth between 2 and 710 mm.

379 **2.2.2. Slope hydrological model**

380 As already pointed out in Section 2.1, the regular geometry of the slope, and the
 381 hydraulic characteristics of the soils, make the flow processes in the soil mantle
 382 mostly one-dimensional. Indeed, A—a simplified 1-D model ~~has~~ had been
 383 previously developed and successfully built, ~~previously~~ validated according to the

384 data collected during the hydrological monitoring activities (Greco et al., 2013;
385 Greco et al., 2018), and was applied to investigate the hydrological response of
386 the slope to synthetic hourly precipitation data. The unsaturated flow through the
387 soil cover-mantle is modelled with 1-D head-based Richards' equation (Richards,
388 1931), assuming for simplicity a single homogeneous soil layer, and it is coupled
389 with a model of the saturated water accumulated in the perched aquifer. The
390 adoption of a 1-D model is allowed thanks to the geometry of the considered soil
391 covermantle, as well as to the prevailing water potential gradients orthogonal to
392 the ground surface when the soil is in unsaturated conditions.

393 The root water uptake has been accounted in the source term of the model,
394 according to the expressions by Feddes et al. (1976), based on estimated potential
395 evapotranspiration, with maximum root penetration depth equal to the soil cover
396 mantle thickness and triangular root density shape.

397 Two boundary conditions are considered for the unsaturated soil covermantle. At
398 ground surface (i.e., the upper boundary condition), if the rainfall intensity is
399 greater than the current infiltration capacity, the excess rainfall forms overland
400 runoff. Otherwise, all rainfall intensity is set as infiltration. The bottom boundary
401 condition links the soil cover-mantle to a perched aquifer developing in the
402 fractures and hydraulically connected to the unsaturated cover through the
403 weathered soil layer (less conductive and capable of retaining much water),
404 located at the contact between the cover and the bedrock. This soil layer
405 penetrates the vertical conduits and fractures (Greco et al., 2013). In this context,
406 the perched aquifer is modelled as a linear reservoir model, that receives water
407 from the gravitational leakage of the overlying unsaturated soil cover-mantle and
408 releases it as deep groundwater recharge and spring discharge (Greco et al.,
409 2018). This conceptualization of the perched aquifer behaviour implies that the
410 streamflow, supplied by the springs, is linearly related to the aquifer water level
411 temporarily developing in the epikarst. Indeed, with this assumption, the model

412 closely reproduces the trend of the stream water level observed in the field (Greco
 413 et al., 2018; Marino et al., 2020a). The pressure head at the soil–bedrock interface
 414 is assumed to follow the fluctuations of the water table of the underlying aquifer.

415 The hydraulic parameters of the soil ~~cover~~ have been obtained from previous
 416 laboratory tests (Damiano and Olivares, 2010) and field monitoring data analysis
 417 (Greco et al., 2013), considering the van Genuchten-Mualem model for the
 418 hydraulic characteristic curves (van Genuchten, 1980). The parameters
 419 describing the hydraulic behaviour of the perched aquifer hosted in the upper part
 420 of the limestone bedrock have been derived from previous studies, which showed
 421 that the model satisfactorily reproduced the fluctuations of water potential and
 422 moisture, observed at various depths in the unsaturated soil cover, both during
 423 rainy and dry seasons (Greco et al., 2013; 2018). Model parameters are
 424 summarized in Table 1~~Table 1~~. The groundwater level of the perched aquifer is
 425 referred to the base of the epikarst, which is assumed 14 m below the soil-bedrock
 426 interface.

427 **Table 1. Hydraulic parameters of the coupled model of the unsaturated soil ~~cover~~**
 428 **mantle and of the aquifer hosted in the ~~Epikarst~~ epikarst** (Greco et al. 2021).

| | | |
|-------------------------------------|---|--------------------|
| | Soil cover <u>mantle</u> thickness (m) | 2 |
| | Saturated water content (-) | 0.75 |
| Soil cover <u>mantle</u> | Residual water content (-) | 0.01 |
| | Air entry value (m^{-1}) | 6 |
| | Shape parameter (-) | 1.3 |
| | Saturated hydraulic conductivity (m/s) | 3×10^{-5} |
| | Epikarst thickness (m) | 14 |
| Epikarst | Effective porosity (-) | 0.005 |
| | Time constant of linear reservoir (days) | 871 days |

429
 430 The equations have been numerically integrated with the finite difference
 431 technique, with a time step of 1 hour over a spatial grid with vertical spacing of
 432 0.02 m.

433 It is important to note that, even if the model simplifies the reality assuming a
434 homogeneous soil profile, a more complex approach considering a layered profile
435 would lead to difficult application of the model at less detailed scales such as
436 regional and catchment scales. Consequently, the hydraulic properties of the
437 homogeneous soil layer should be considered as effective properties, useful to
438 reliably reproduce the observed phenomena.

439 **2.2.3. Synthetic hydrometeorological data**

440 As it has been stated from previous sections, the dataset comes from the
441 simulation of the hydrologic response of a slope to 1000_-years long hourly
442 rainfall time series, carried out with a physically based model, calibrated for the
443 case study. The output contains the time series of soil water content and suction
444 at all depths throughout the soil ~~cover~~mantle, of the water exchanged between
445 the soil and the atmosphere, of the leakage through the soil-bedrock interface,
446 and of the predicted water level of the underlying aquifer.

447 One hour before the onset of each rainfall event, the following variables have
448 been extracted, as they would be measurable in the field and are representative
449 of antecedent conditions: the aquifer water level (h_a), the mean volumetric water
450 content in the uppermost 6 cm of soil ~~cover~~mantle (θ_6) and the mean volumetric
451 water content in the uppermost 100 cm of soil ~~cover~~mantle (θ_{100}). To quantify
452 the effects of rainfall on the slope response, the change of the water stored in the
453 soil ~~cover~~mantle at the end of each rainfall event (ΔS) has been computed and
454 compared with the total rainfall depth of the event (H).

455 Specifically, the inclusion of soil water content information has been chosen, as
456 it can be obtained from available satellite-derived remote sensing products
457 (Paulik et al., 2014; Pan et al., 2020; ~~Paulik et al., 2014~~) or from field sensor
458 networks (Wicki et al., 2020). Regarding satellite products, in many cases not

459 giving precise water content values, they satisfactorily reproduce temporal
460 trends, which represent a valuable information for hazard assessment.

461 Besides, as the model introduces a linear relationship to estimate the outflow
462 from the groundwater system, the monitored stream water level has been
463 considered comparable to the simulated groundwater level, as the two variables
464 are assumed directly proportional in the model.

465 **2.3. Data analysis techniques**

466 The resulting dataset has been analyzed with Machine Learning techniques,
467 aiming at capturing the complex interactions between the hydrological
468 subsystems (i.e., soil ~~cover~~mantle, fractured bedrock, surface water). Indeed, the
469 analysis of the data is not only constrained to classical statistical analyses, such
470 as data frequency distributions, but also to data classification based on their
471 geometrical distribution, and on quantifying the importance of the considered
472 antecedent variables on the simulated response as well.

473 **2.3.1. Variable importance assessment by Random Forest**

474 The Random Forest is a Machine Learning method that sets its basis on the theory
475 of regression/classification trees, bagging data and capturing even the complex
476 or non-linear interactions in-between the data of a set with relatively low bias
477 (Breiman, 2001). This method is often used to forecast a desired variable based
478 on predictor variables in terms of regression or classification set of randomly
479 constructed trees. In this case, a regression based Random Forest technique is
480 applied to predict the ~~slope-soil storage~~ response (ΔS) at the end of each rainfall
481 event of total depth H , using as predictors all possible triplets of variables
482 described in the section 2.2.3 (~~$H_{\text{total-rainfall-depth}}$, h_a aquifer water level,~~
483 ~~θ_6 mean volumetric water content in the uppermost 6 cm and θ_{100} mean~~
484 ~~volumetric water content in the uppermost 100 cm): Specifically, four Random
485 Forest models have been developed: RF1 with input features $\langle H, \theta_6, h_a \rangle$, RF2,~~

486 with input features $\langle H, \theta_{100}, h_a \rangle$, RF3, with as input features $\langle H, \theta_6, \theta_{100} \rangle$ and RF4
487 with input features: $\langle H, \theta_6, \theta_{100} \rangle$. The 80% of the dataset was used to train the
488 models and tuning the major hyperparameters of random forest algorithm: the
489 number of trees, the maximum depth, the minimum sample leaf, and the
490 maximum number of feature (more details about the evaluation and optimization
491 of the hyperparameters are provided in Appendix B).~~A total of 100 trees with a~~
492 ~~maximum leaf split of 20 nodes have been built for all variable combinations and~~
493 ~~trained with the 80% of the dataset randomly selected to obtain different regressor~~
494 ~~models.~~

495 Then, the best ~~triplet of~~ predictor triplet of variables is selected according to the
496 lowest value of the Root Mean Squared Error (RMSE) calculated using the test
497 data set consisting of the 20% of the remaining data.

498 Furthermore, to understand how a single variable affects the regression model,
499 the predictor importance is measured by the sensitivity of Random Forest model
500 to the predicted variable (i.e., soil ~~cover~~ mantle response), which is proportional
501 to the RMSE, by permuting on purpose the variables between the levels of the
502 model and ~~calculating~~ estimating the corresponding change in the RMSE. Hence
503 the most important variable is the one that exhibits the greatest change in RMSE
504 after the permutations (Hastie et al., 2008). ~~Hence, the importance of predictor~~
505 ~~variables follows the magnitude of the change in RMSE. This feature is usually~~
506 ~~referred to in relative terms to the most important variable, called variable relative~~
507 ~~importance (Hastie et al., 2008).~~

508 **2.3.2. Data classification by clustering analysis**

509 The exploratory analysis of spatial large datasets is often performed by means of
510 clustering techniques, aiming at identifying different classes in the data,
511 accounting on the distribution of the variables under study. There are two types
512 of clustering algorithms used for class identification purposes: algorithms based

513 on the density of points and algorithms based on the distance between points. The
514 algorithm used here is named k-means, and it is a distance-based procedure to
515 cluster data, based on the number of desired clusters and their centroids. The
516 algorithm ~~assigns every element in the dataset to a cluster, proceeds to~~ iteratively
517 ~~minimize-minimizing~~ the variance of the Euclidean distance of ~~the elements of~~
518 ~~each~~ cluster ~~elements~~ from their centroids, ~~by accordingly moving these latter~~.
519 Consequently, the data labelling is done based on their geometrical disposition in
520 the ~~studied plane or spacedot cloud~~, depending on the target number of clusters
521 to be identified (Lloyd, 1982; Arthur and Vassilvitskii, 2007). When variables
522 with very different magnitudes are being related for clustering purposes, it is
523 convenient to normalize the data keeping the relative distances between
524 observations. Therefore, the clustering here is applied to the standardized data to
525 exploit the variance of each variable and keeping the geometrical disposition
526 between observations stable.

527 As the k-means algorithm does not automatically estimate the optimal number of
528 clusters to be identified within the dataset, the Silhouette metric has been used
529 here to evaluate the preferred number of clusters (Rousseeuw, 1987; de Amorim
530 and Hennig, 2015). In fact, this metric quantifies the quality of cluster
531 identification by scoring the difference between the overall average intra-cluster
532 distances and the average inter-cluster distances related to the maximum between
533 the latter two. In that way the metric would always be a value ranging from -1
534 and 1, where typically 1 means that clearly distinguished clusters have been
535 identified, 0 means that the identified clusters are indifferent, and -1 means that
536 data are mixed in the identified clusters.

537 **3. Results and discussion**

538 The analysis is ~~developed-carried out~~ on both field monitored and synthetic
539 datasets, to quantify the information provided by the defined antecedent variables
540 useful to predict the seasonal changes of the slope response to precipitations.

541 **3.1. Role of measurable variables on the slope-response of the soil**
 542 **mantle**

543 To select the most appropriate-informative triplets of predictor-variables, four
 544 Random Forest models for predicting the change in water storage (ΔS) in the soil
 545 covermantle, associated to rainfall events of total depth H, four Random Forest
 546 models are trained to predict the ratio $\Delta S/H$, based on the dataset consisting of
 547 all possible combinations of the synthetic variables: $\langle H, \theta_6, h_a \rangle$, $\langle H, \theta_{100}, h_a \rangle$,
 548 $\langle H, \theta_6, \theta_{100} \rangle$ and $\langle \theta_6, \theta_{100}, h_a \rangle$. In fact, the change in storage ΔS is obviously
 549 strongly dependent on the event rainfall depth H (i.e., the more it rains the more
 550 soil storage increases), thus concealing important hydrological processes going
 551 on the slope. Differently, the choice of the ratio $\Delta S/H$, a measure of the amount
 552 of rain that remains stored in the soil mantle, allows detaching the water drainage
 553 processes from the water accumulation processes. For each Random Forest
 554 model, the values of the Root Mean Square Error (RMSE) are calculated, and the
 555 importance of each predictor variable is evaluated according to the procedure
 556 described in Section 2.3.1. The computational effort implied in doing the
 557 calculations by a conventional workstation with a Core(TM) i7-10870H
 558 processor and 16 GB of SDRAM memory is less than 2 minutes for each model
 559 run. The obtained results are reported in Table 2.

560 **Table 2. RMSE and variable importance for H , θ_6 , θ_{100} and h_a in the prediction**
 561 **of soil response described as ΔS**

| Dataset | RMSE | Importance | | | |
|---|--------|------------|------------|----------------|-------|
| | | H | θ_6 | θ_{100} | h_a |
| $\langle H, \theta_6, h_a \rangle$ | 5.353 | 0.963 | 0.024 | - | 0.012 |
| $\langle H, \theta_{100}, h_a \rangle$ | 4.336 | 0.964 | - | 0.024 | 0.010 |
| $\langle H, \theta_6, \theta_{100} \rangle$ | 4.706 | 0.962 | 0.014 | 0.022 | - |
| $\langle \theta_6, \theta_{100}, h_a \rangle$ | 24.665 | - | 0.313 | 0.340 | 0.345 |

562

As it could be seen from Table 2, an expected behavior on the slope response, quantified as ΔS , answers back highly depending on the rainfall amount as the most important variable in the triplet, while the antecedent conditions show an almost negligible importance with less than 3%. Additionally, the absence of total rainfall among the predictors leads to a substantial increase in the RMSE (24.665). This result is physically expected; the more it rains the more the water storage in the slope increases. Nevertheless, such strong relationship between H and ΔS could conceal important hydrological processes going on the slope. For this reason, normalization schemes could be introduced to account different processes in the slope response. In this case the ratio $\Delta S/H$ is used as a measure of the association between the amount of rain and how much it was stored in the soil cover, pursuing to detach the water drainage processes from the water accumulation processes. To this end, additional Random Forest models are trained on the same four datasets for predicting the normalized water storage in slope $\Delta S/H$.

Table 23. RMSE and variable importance for H , θ_6 , θ_{100} and h_a in the prediction of soil response described as $\Delta S/H$

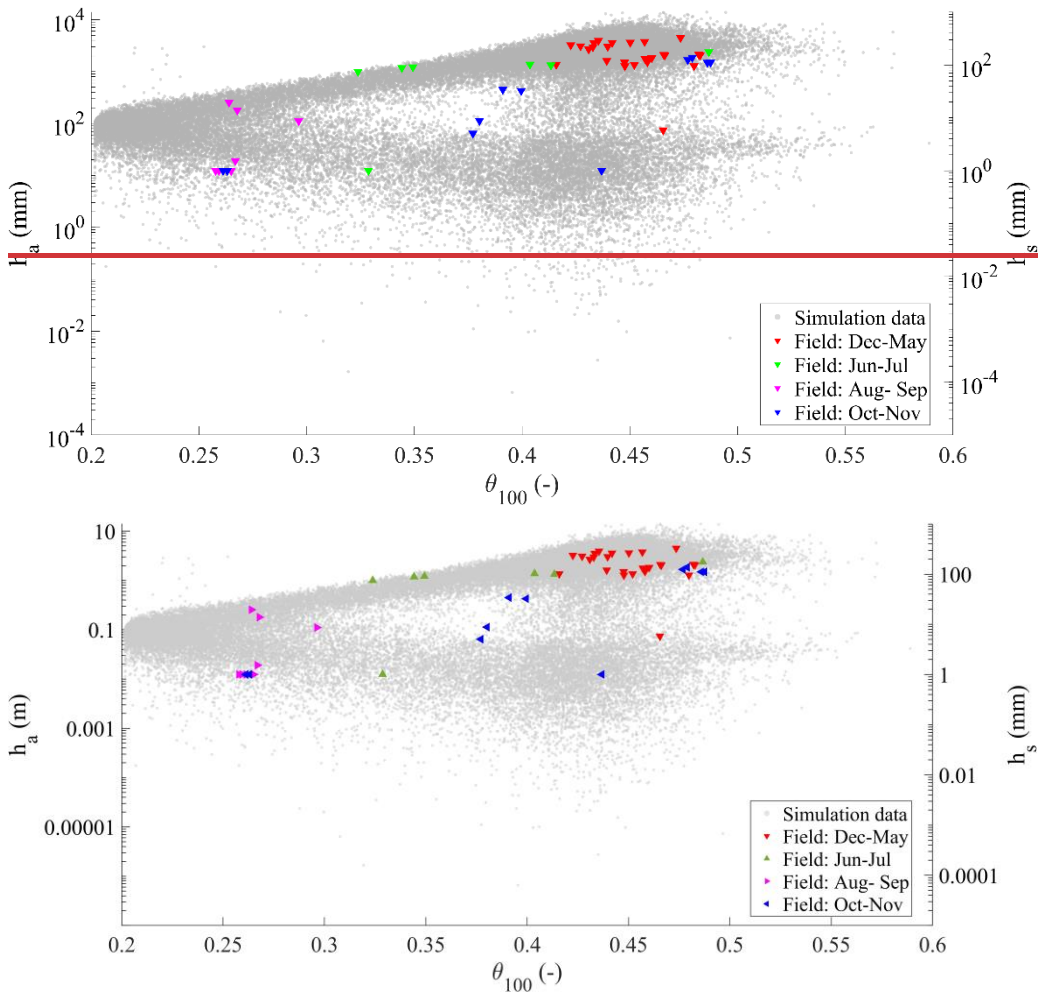
| Dataset | RMSE | Importance | | | |
|---|-------|------------|------------|----------------|-------|
| | | H | θ_6 | θ_{100} | h_a |
| $\langle H, \theta_6, h_a \rangle$ | 0.213 | 0.352 | 0.329 | - | 0.319 |
| $\langle H, \theta_{100}, h_a \rangle$ | 0.197 | 0.293 | - | 0.405 | 0.302 |
| $\langle H, \theta_6, \theta_{100} \rangle$ | 0.203 | 0.340 | 0.261 | 0.399 | - |
| $\langle \theta_6, \theta_{100}, h_a \rangle$ | 0.210 | - | 0.292 | 0.414 | 0.293 |

All the choices of triplets indicate that all the tested variables are similarly informative to predict the Normalizing-normalized the slope soil mantle response

584 $\Delta S/H$ as $\Delta S/H$ (Table 2Table 3) highlights the important role played by the other
585 variables. It is worth to note the importance of the perched ground water level,
586 which can be compared with the importance of the ~~two soil~~ water contents and
587 of the total rainfall depth. The importance of h_a on the slope response of the soil
588 mantle suggests that, the presence of in some conditions, of the change in soil
589 storage ~~less connected to rainfall values and more linked to~~ is affected by the
590 capability effectiveness of water exchange between the soil mantle and the
591 underlying aquifer ~~and the soil cover~~, as it will be discussed in the following
592 sections. Moreover, in Table 2Table 3 the ~~variables with triplet showing~~ the
593 lowest RMSE values ~~are is conformed by the~~ total rainfall depth, the aquifer
594 water level and the mean volumetric water content in the uppermost 100 cm.
595 According to the Random Forest model, they are the most informative for
596 predicting the slope-soil mantle response. Therefore, the triplet $\langle H, \theta_{100}, h_a \rangle$ is
597 used for further analysis.

598 **3.2. Underground Soil and underground antecedent conditions**

599 The field monitoring activities allow to get a complete dataset that traces the
600 rainfall values coupled with the soil mean volumetric water content in the
601 uppermost meter of the soil profile (θ_{100}) and the water depth of the Castello
602 stream (h_s), both measured hourly for three years. The field monitored data,
603 composed by 57 rainfall events, include the water level of the Castello stream
604 rather than the direct measurement of the aquifer water level (h_a). Nevertheless,
605 a direct relationship links the water level in the aquifer and the water level in the
606 stream, as assumed for the mathematical modelling. This dataset has been
607 enriched synthetically, as it has been described in section 2.2.

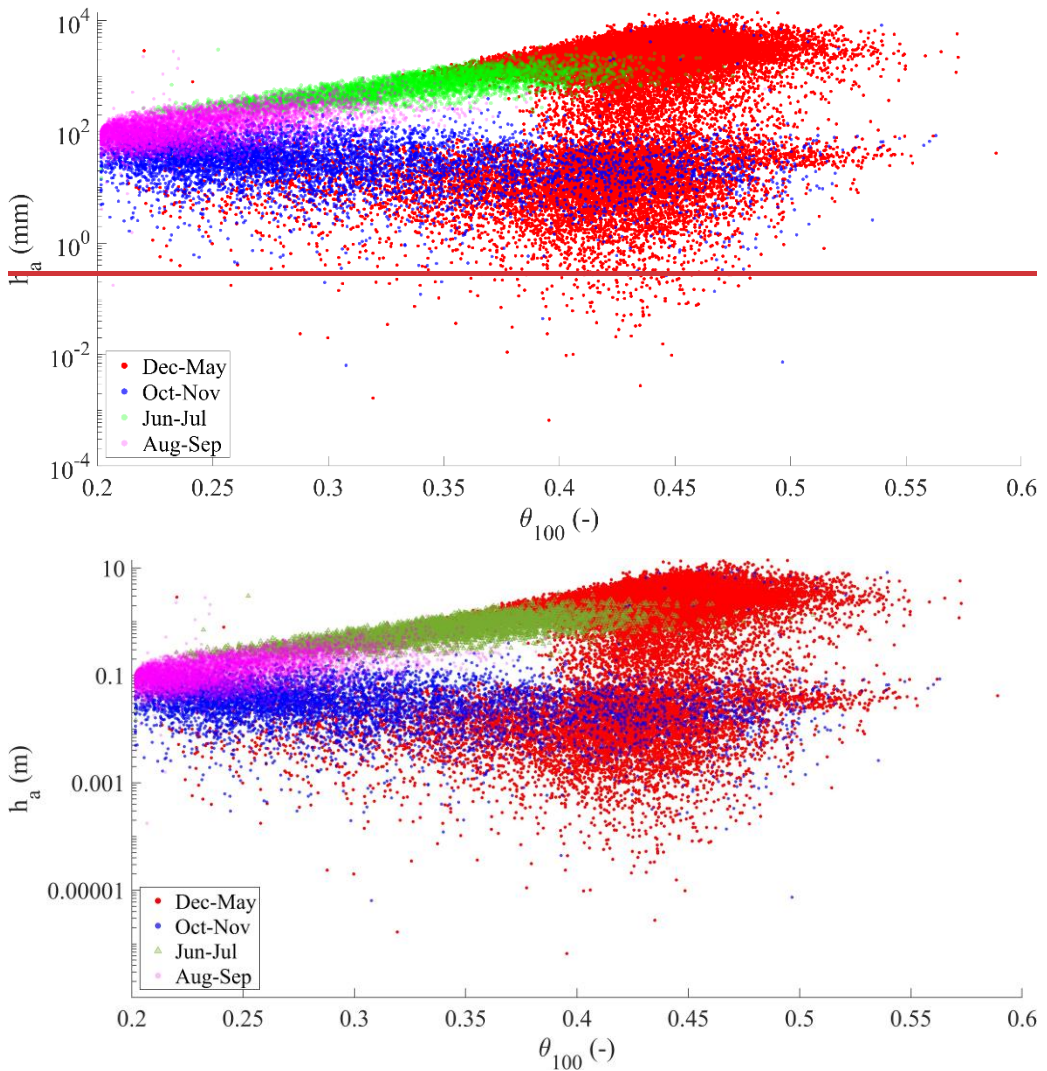


610 **Figure 5.** Field monitored mean volumetric water content in the upper meter of the
 611 soil profile (θ_{100}) and water depth in the Castello stream (h_s) compared with
 612 simulated data (the vertical axis is plotted in logarithmic scale to help visualizing of
 613 small water levels).

614 Therefore, to analyze the effects of the underground conditions on the slope
 615 response, ~~Figure 5~~ [Figure 5](#) shows the simulated data (circular dots in the
 616 background) and the field monitored data (triangular colored dots). Logarithmic
 617 axes are used to distinguish the very low aquifer water level from the high values.

618 Four major seasonally recurrent conditions could be identified for the water in
 619 the subsurface system from field monitored data: first, a condition usually
 620 occurring between December and May is characterized by the highest water

621 content in the soil and the highest measured water level in the stream. Second,
622 the period from June to July is characterized by intermediate water content
623 values, with still high level in the stream. Third, the period from August to
624 September is characterized by the lowest values of water content in the soil, but
625 also the lowest water depth h_s measured in the stream (few centimeters, in some
626 cases nearly zero). Finally, the period from October to November is characterized
627 by a wide range of values in soil water content and a relatively low range of
628 stream water depth.



629
630
631 **Figure 6.** Seasonal behavior of the aquifer water level (h_a) and the mean
632 volumetric water content of the upper meter of the soil profile (θ_{100}) for the
633 synthetic dataset (the vertical axis is plotted in logarithmic scale to help
634 visualizing small water levels).

635 The underground antecedent conditions are naturally linked to a seasonal
636 behavior dominated by the hydrological conditions which can be traced in time
637 as it can be seen from the synthetic data (Figure 6). The months from
638 December to April follow a winter and spring behavior, characterized by wet soil
639 conditions and aquifer water levels ranging from low to high. From June to July,
640 a late spring behavior is visible, characterized by relatively dry soil (i.e., most of

641 the data falling below soil field capacity), in combination with relatively high
642 groundwater levels (indicating a still active slope drainage). In August and
643 September, a summer like behavior is shown, with the driest soil water content
644 and generally low aquifer water level. Finally, in October and November, the end
645 of the dry season is shown: a wide range of soil wetness coupled with a still low
646 aquifer water level.

647 For both the field monitored and synthetically obtained datasets, the observed
648 conditions are the result of the time lag between the beginning of the rainy season
649 and the slope response. The recurrent seasonal behavior observed for the
650 synthetic dataset, although delayed or anticipated owing to the year-by-year
651 variability of rainfall, is close to that observed in the field.

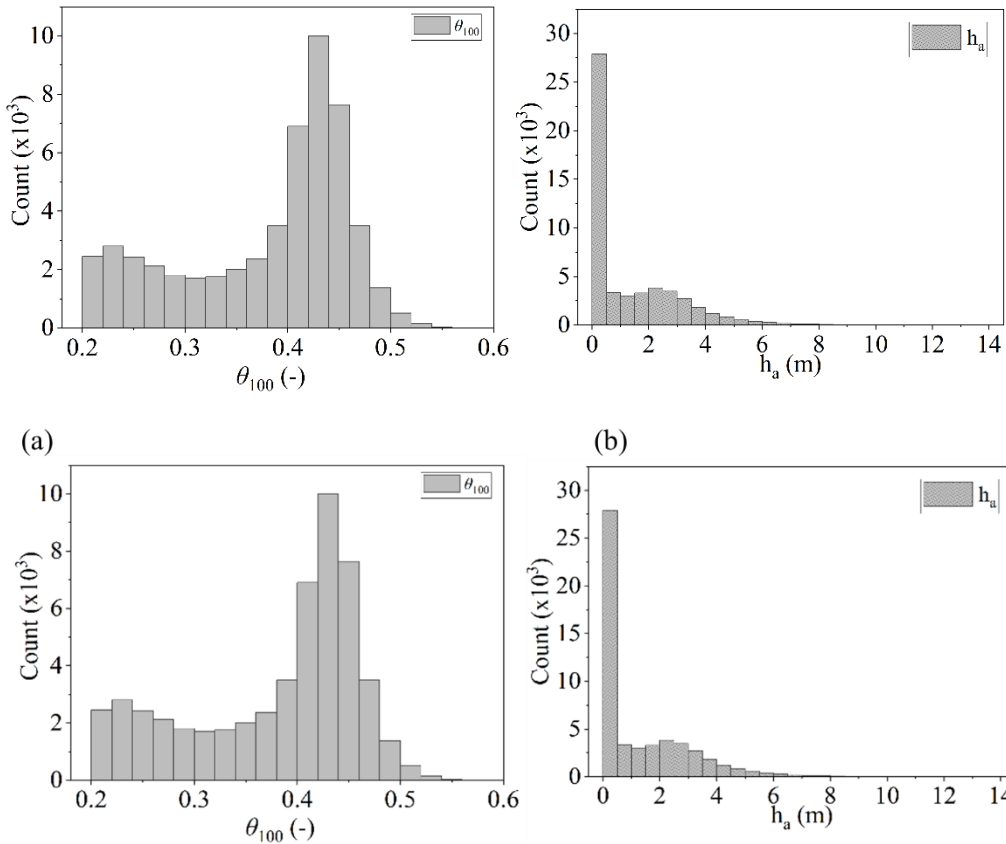
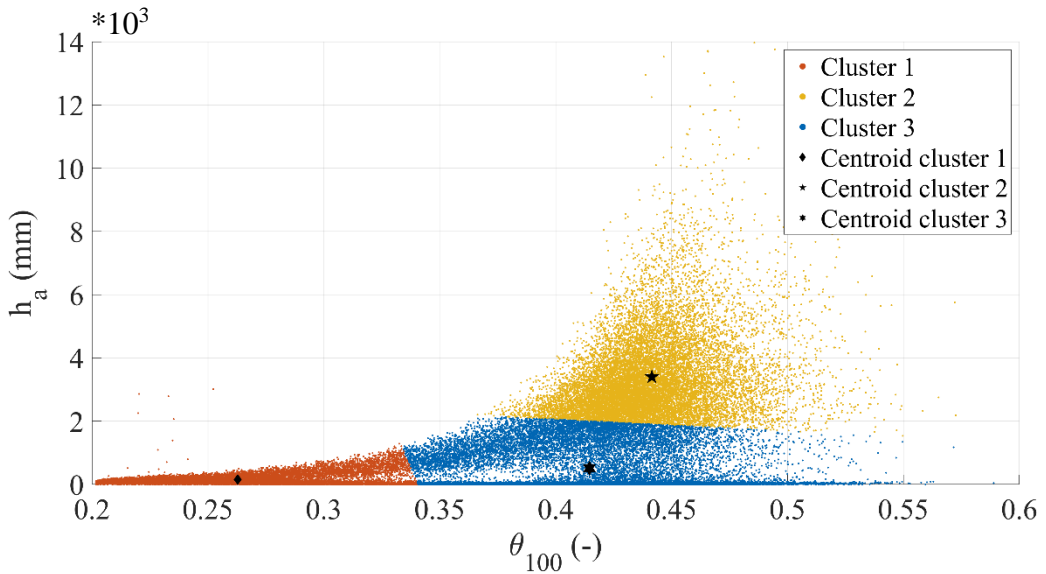


Figure 7. Histograms for data distributions of (a) θ_{100} (left) and (b) h_a (right) for the synthetic dataset

The overall situation for the synthetic dataset of antecedent conditions (i.e., duplets $\langle \theta_{100}, h_a \rangle$) can be described by the distribution of each individual variable, which can be seen in the histograms shown in [Figure 7](#). It is interesting to note that, for both θ and h_a , a bimodal behaviour is observed, corresponding to dry and wet field conditions.

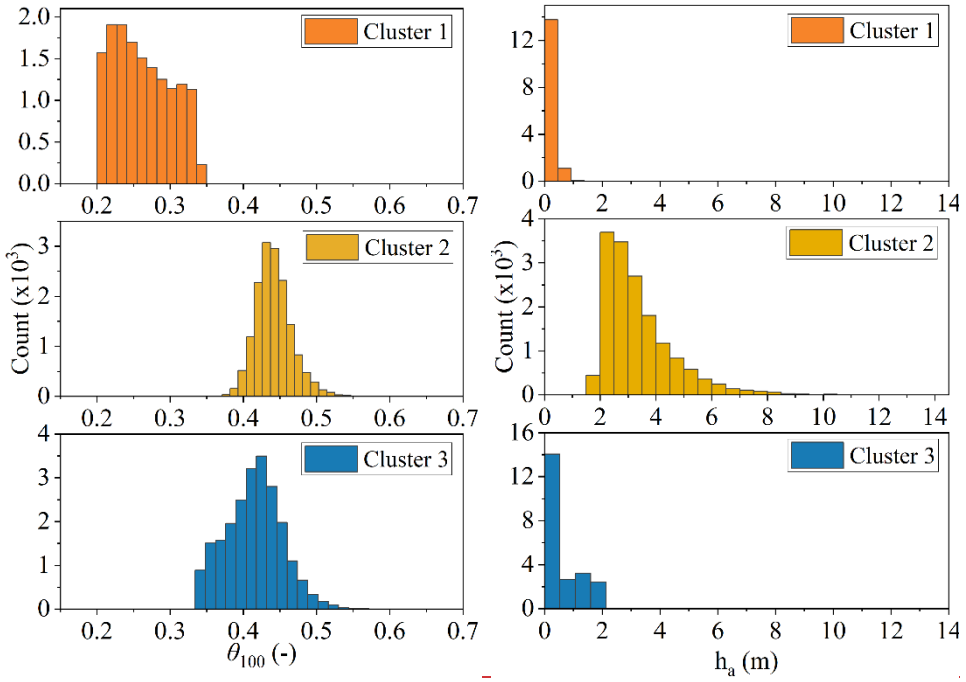


661

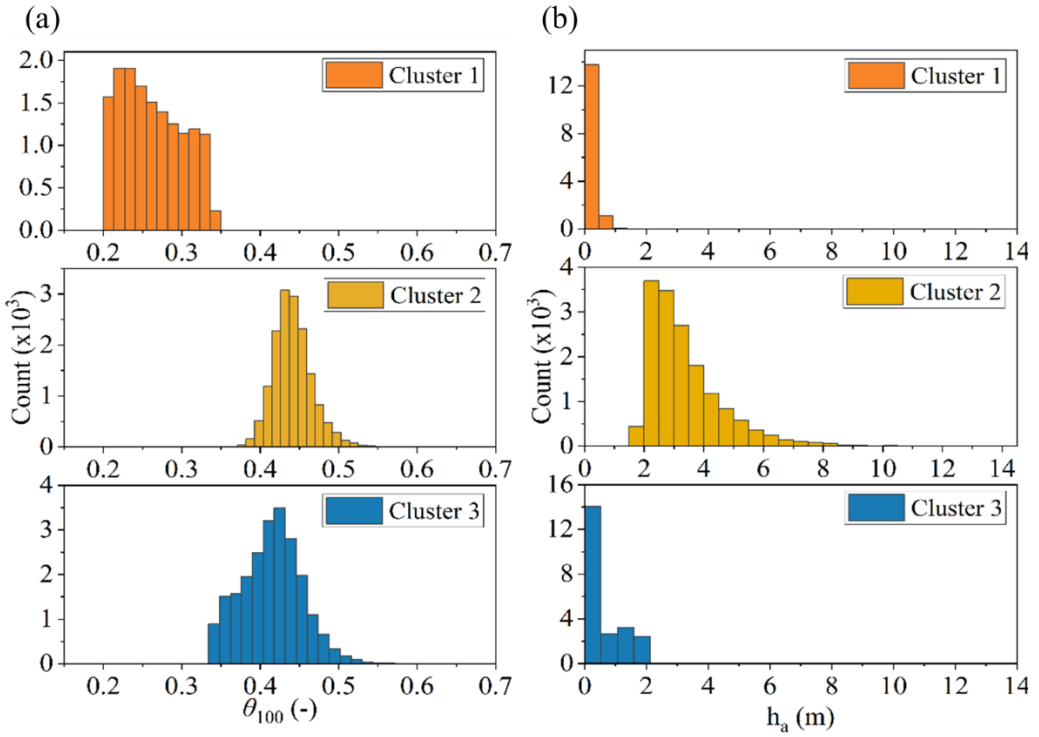
662 **Figure 8. Identified clusters for the duplets $\langle \theta_{100}, h_a \rangle$ representing underground**
 663 **antecedent conditions of the synthetic dataset. For each cluster, the centroids are**
 664 **shown.**

665 The k-means clustering technique has been used to investigate the geometrical
 666 distribution of the duplets $\langle \theta_{100}, h_a \rangle$, with number of clusters ranging from 2 to
 667 7. According to the Silhouette metric, the optimal number of clusters is 3, with a
 668 metric value of 0.7, allocating the 28%, 30% and 42% of the data in clusters 1, 2
 669 and 3 respectively. [Figure 8](#) shows the 3 clusters obtained within the
 670 synthetic dataset. Centroid positions are also displayed, showing the zones of the
 671 clouds where most of the dots are gathered. This representation of the data use
 672 both vertical and horizontal axes in linear scale to let visualize distance
 673 magnitudes between the different clusters, but it corresponds to the same dataset
 674 shown in [Figure 6](#).

675 The distribution of the data after clustering is also analyzed for each cluster and
 676 the histograms are shown in [Figure 9](#). It looks clear that the clusters
 677 capture different couplings of dry and wet underground antecedent conditions.



678



679

680 **Figure 9.** Histograms for data distributions of (a) θ_{100} (left) and (b) h_a (right)
 681 according to each identified cluster in the duplets (θ_{100}, h_a)

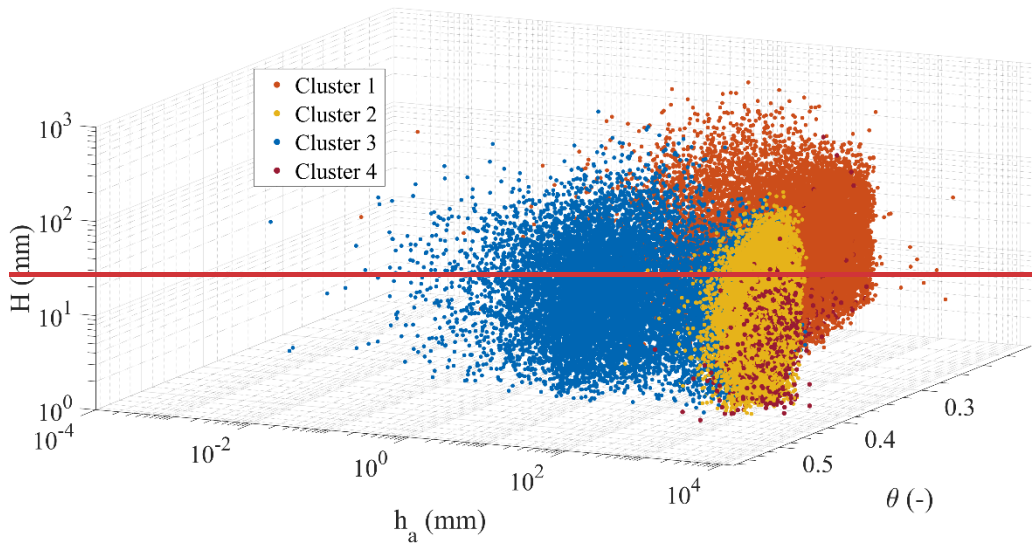
682 In fact, cluster 1 captures dry conditions, with a volumetric water content below
683 the field capacity θ_{fc} (it was estimated as 0.35 with the empirical relationship
684 proposed by Twarakavi et al. (2009) according to the van Genuchten model
685 parameters) and low values of h_a . Differently, clusters 2 and 3 capture scenarios
686 related to relatively wet soil ~~eover-~~mantle conditions (i.e., $\theta_{100} > \theta_{fc}$), coupled
687 to low h_a in cluster 3, gathering scenarios normally observed in late autumn, and
688 to the highest h_a conditions for cluster 2, comprising conditions normally
689 occurring in late winter and spring.

690 The two chosen variables, θ_{100} and h_a , allow identifying three different
691 antecedent slope conditions one hour before the onset of any rainfall event.
692 Hence, it is worthy to investigate how these different antecedent conditions may
693 be related to different slope responses to precipitations.

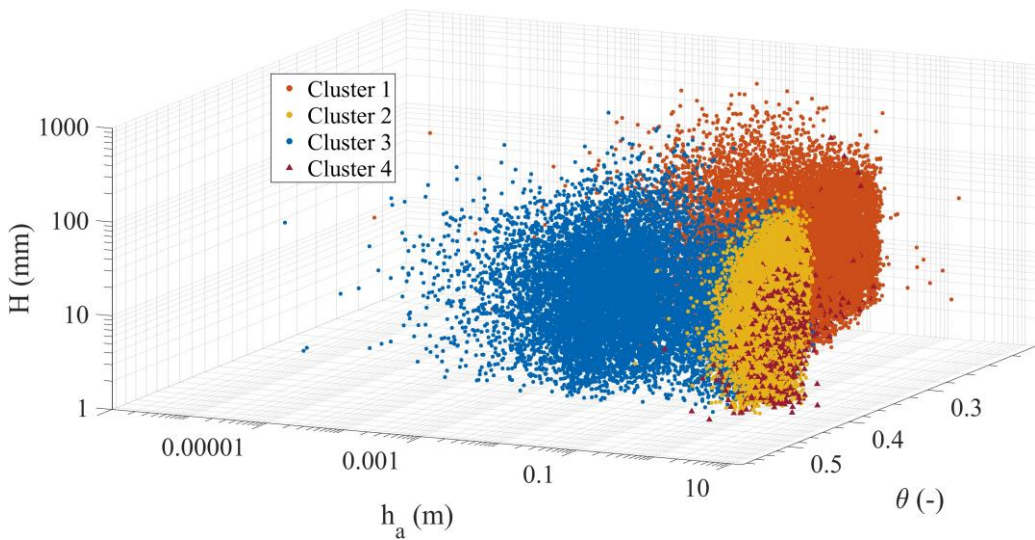
694 **3.3. Effects of ~~underground-~~soil and underground antecedent** 695 **conditions on the slope response to rainfall**

696 The analysis of the data has been focused on identifying clusters within the
697 triplets $\langle \theta_{100}, h_a, \Delta S/H \rangle$, aiming to evaluate the slope response as the amount of
698 rainwater being stored/draind in the soil ~~eover-~~mantle. The results are being
699 plotted in the space composed by the variables that can be monitored in the field:
700 (θ_{100}, h_a, H) .

701 As it is not always expected to experience increased soil storage during rainfall
702 events, the identification of draining slope conditions is an important aspect.



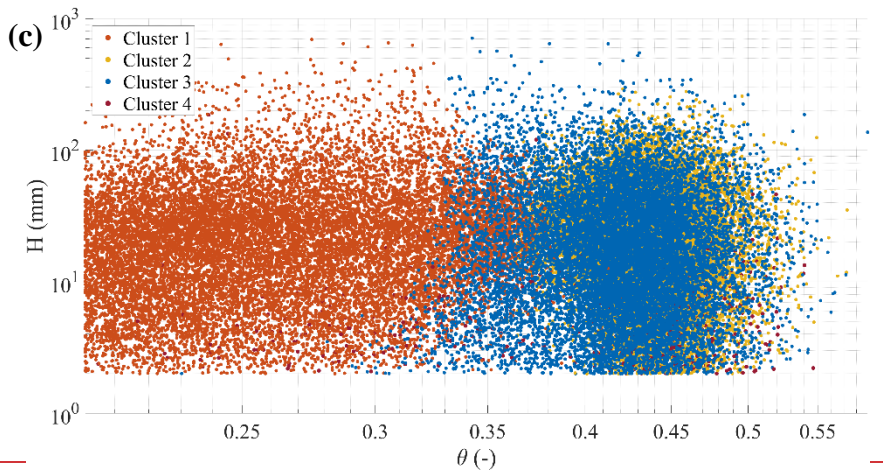
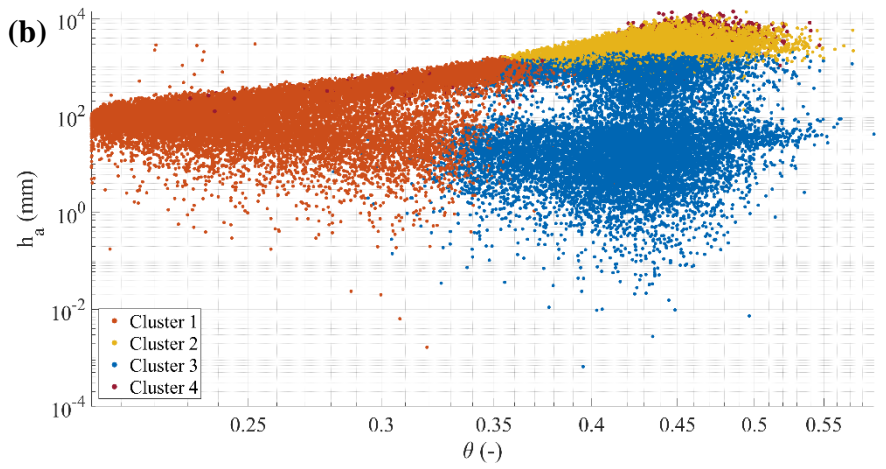
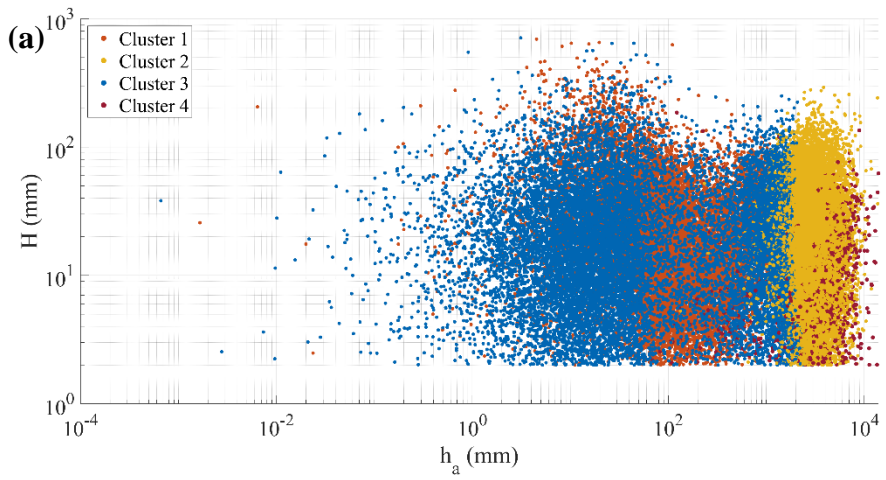
703

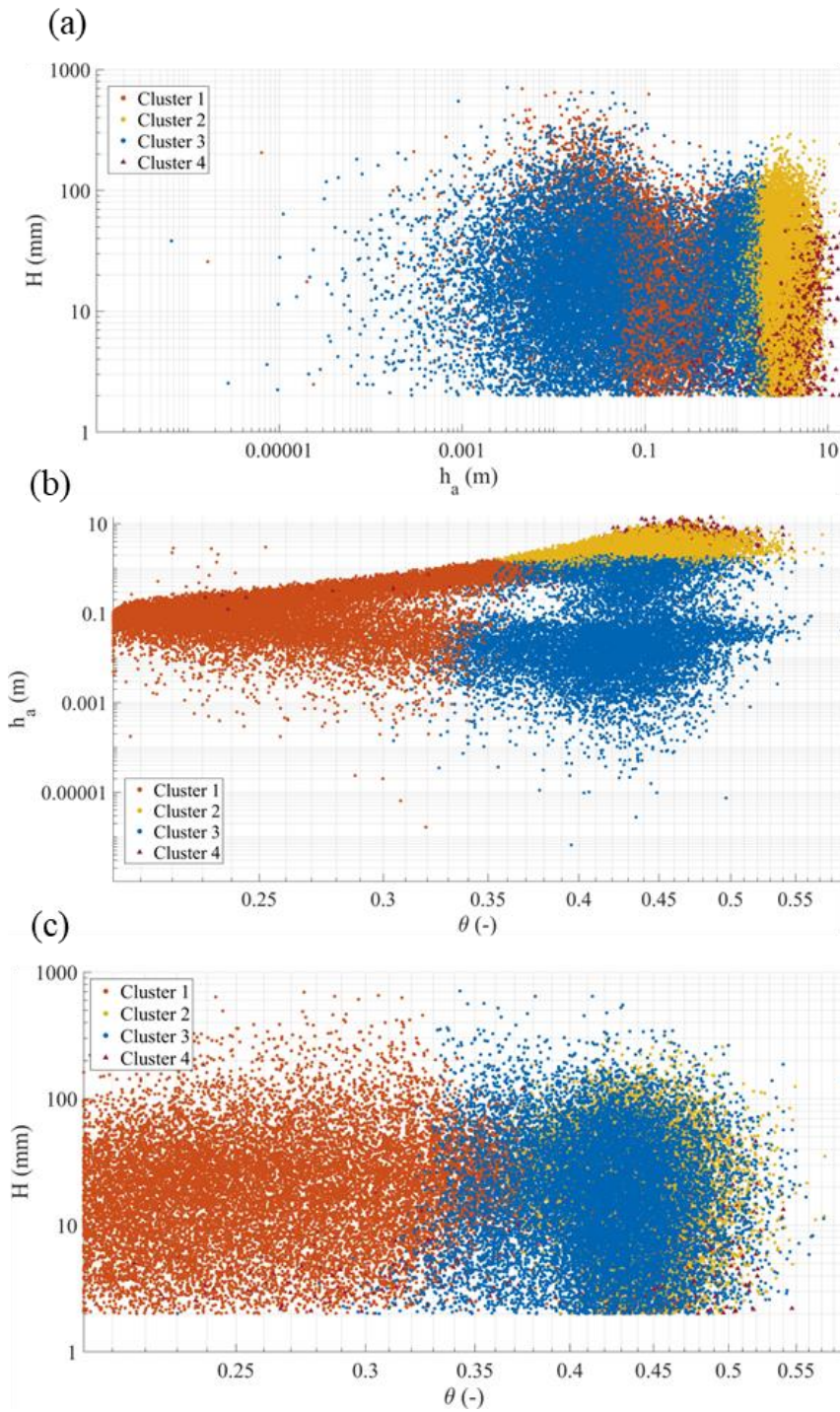


704

705 **Figure 10.** Clustering results of the synthetic data triplets $\langle \theta_{100}, h_a, \Delta S/H \rangle$
 706 represented in the space (θ_{100}, h_a, H)

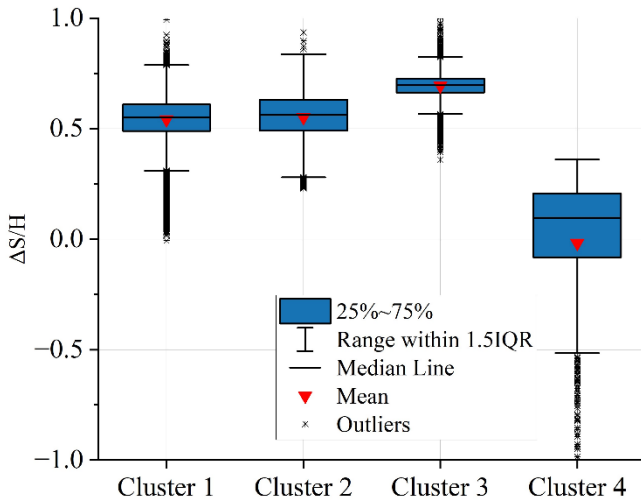
707





709
710 **Figure 11.** Clustering results of the triplets $\langle \theta_{100}, h_a, \Delta S/H \rangle$ in (a) (θ_{100}, h_a)
711 plane; (b) (θ_{100}, H) plane; (c) (H, h_a) plane

712 [Figure 10](#) and [Figure 11](#) show the data clusters for the triplets
 713 $\langle \theta_{100}, h_a, \Delta S/H \rangle$, for any identified rainfall event, represented in the (θ_{100}, h_a, H)
 714 space in a logarithmic axis representation. The Silhouette metric in this case
 715 suggests 4 as an optimal number of clusters with a metric value of 0.61. It is
 716 remarkable that three of the clusters are close to those already identified from the
 717 antecedent (seasonally recurrent) underground conditions (section 3.2).



718 **Figure 12. Distribution of the slope response $\Delta S/H$ for the data in each cluster**
 719 Specifically, cluster 1, 2 and 3 correspond to different slope processes according
 720 to $\Delta S/H$ ([Figure 12](#)). Even if cluster 1 and cluster 2 show similar
 721 responses, with slightly smaller $\Delta S/H$ for cluster 1, the controlling processes are
 722 indeed different; the conditions of cluster 1 are typically occurring in dry seasons
 723 with long dry periods between short rainfall events, leading to dry antecedent
 724 conditions, so that accumulation of water in the soil cover-mantle (increase in
 725 water storage) is expected at each event. The data in cluster 2 are typically related
 726 to wet seasons, especially in late winter and spring, where rainfall events are more
 727 frequent, leading to antecedent wet soil ($\theta_{100} \geq \theta_{fc}$) and antecedent high ground
 728 water level. However, these conditions do not seem to correspond to effective
 729 slope drainage, so that the slope response in cluster 2 results comparable to that
 730

731 observed in cluster 1 in terms of $\Delta S/H$. Instead, the conditions gathered in cluster
732 3 differ from those in cluster 2 for the lower aquifer water level h_a , and the
733 highest $\Delta S/H$ indicates the lowest slope drainage.

734 The additional cluster 4 identified here highlights a particular slope response, as
735 it catches all the conditions where nearly zero and negative ΔS take place,
736 meaning an effective slope drainage during rainfall events. It is interesting to note
737 that, even for relatively high rainfall events (above 100 mm), this slope response
738 occurs when soil moisture is above the field capacity and when this condition is
739 coupled with very high groundwater level, probably due to the high permeability
740 all along the soil ~~cover~~-mantle and to the hydraulic connection with the
741 underlying aquifer.

742 4. Conclusions

743 This study aims at identifying and analysing the major hydrological controls of
744 the slope response to precipitations and, in that way, defining suitable variables
745 to be monitored in the field to predict such response. The studied case refers to
746 the hydrological processes in a slope system consisting of a pyroclastic soil ~~cover~~
747 mantle overlaying a fractured karstic bedrock, where a perched aquifer develops
748 during the rainy season. A synthetic time series of slope response to precipitations
749 has been built, thanks to a physically based model, previously calibrated with
750 field monitoring data, coupled with a stochastic rainfall generator. ~~The seasonal~~
751 ~~behaviour of the slope shows substantial agreement between~~ Synthetic and
752 experimental data show substantial agreement. In fact, the soil water content
753 values measured in the field are close to those of the synthetic dataset.
754 Furthermore, the simulated epikarst water level shows similar seasonal behaviour
755 as the stream level records, indeed directly related with the discharge from the
756 epikarst aquifer. The synthetic dataset has been explored with Random Forest
757 and k-means clustering, to evaluate the slope response characterized as the
758 change in water stored in the soil ~~cover~~-mantle (ΔS) during precipitation events

759 with rainfall depth H , starting from different underground antecedent conditions.
760 These were quantified through the mean volumetric water content in the
761 uppermost meter of soil ~~cover~~ mantle (θ_{100}) and the aquifer water level (h_a), one
762 hour before the onset of rainfall.

763 The ratio $\Delta S/H$, which allows identifying slope response regardless the amount
764 of event precipitation, is sensitive to both h_a and θ_{100} , with the groundwater level
765 being the most influential antecedent variable. The underground antecedent
766 conditions, characterized by θ_{100} and h_a and linked to the seasonal
767 meteorological forcing, allow identifying different slope responses, related to the
768 seasonally active hydrological processes.

769 High perched groundwater level, typical of winter and spring, indicates active
770 slope drainage, which compensates rainwater infiltration, so that the soil storage
771 remains stable, or even reduces, even after large rainfall events.

772 Differently, low perched groundwater level corresponds to impeded slope
773 drainage. When it occurs with initially dry soil ~~cover~~ mantle (typically in summer
774 and early autumn), it tends to retain all the infiltrated rainwater as increased soil
775 storage. When the soil ~~cover~~ mantle is already wet (i.e., above the field capacity)
776 at the onset of rainfall events, as it usually happens in late autumn and early
777 winter, the increase of soil storage is smaller, as the soil approaches saturation.

778 The presented results suggest that monitoring antecedent conditions, by
779 measuring suitable variables to identify the major hydrological processes
780 occurring in the slope in response to precipitations, can be useful to understand
781 such processes and to develop effective predictive models of slope response.
782 Therefore, the proposed methodology can be replicated also in other contexts and
783 be useful for several hydrologic applications: from the water supply towards
784 natural streams due to infiltrated water, to the hydric stress estimation in crops
785 (e.g., the centenary chestnut forests ~~in the area~~ of the case study) especially in

786 very dry seasons, but also for the design of effective monitoring networks
787 exploiting geohydrological information for geohazard prevention (and early
788 warning).

789

790 **Appendix A: Calibration of the Stochastic Rainfall Generator**
791 The Neyman-Scott Rectangular Pulse (NSRP) model (Neyman and Scott, 1958;
792 Rodriguez-Iturbe et al., 1987; Cowpertwait et al., 1996) is here used as stochastic
793 rainfall generator. The NSRP describes the process of point rainfall as a
794 superposition of randomly arriving rain clusters, each containing several rain
795 cells with constant intensity. The hyetograph within a cluster is obtained by
796 summing the intensity of the various cells belonging to the cluster. It has been
797 calibrated based on 17 years of experimental data (2000-2016) of rainfall depth
798 at 10 min time resolution, recorded by the rain gauge managed by the Civil
799 Protection in Cervinara (Southern Italy). The calibration has been carried out by
800 minimizing, for rainfall aggregated at various durations, the difference between
801 the following quantities, estimated by the model and calculated from the
802 experimental data: mean, variance, lag 1 autocorrelation, probability of dry
803 interval, probability of transition from dry-to-dry interval and probability of
804 transition from wet-to-wet interval. The calibration procedure, based on the one
805 proposed by Coptwertwait et al. (1996), is described in detail in Peres and
806 Cancelliere (2014). To account for the seasonality of rainfall, these quantities
807 have been calculated month by month in the experimental record (Figure A1),
808 suggesting that the calibration of the NRSP model should be carried out
809 separately for seven homogeneous periods (September, October, November,
810 December-March, April, May-June, July-August).

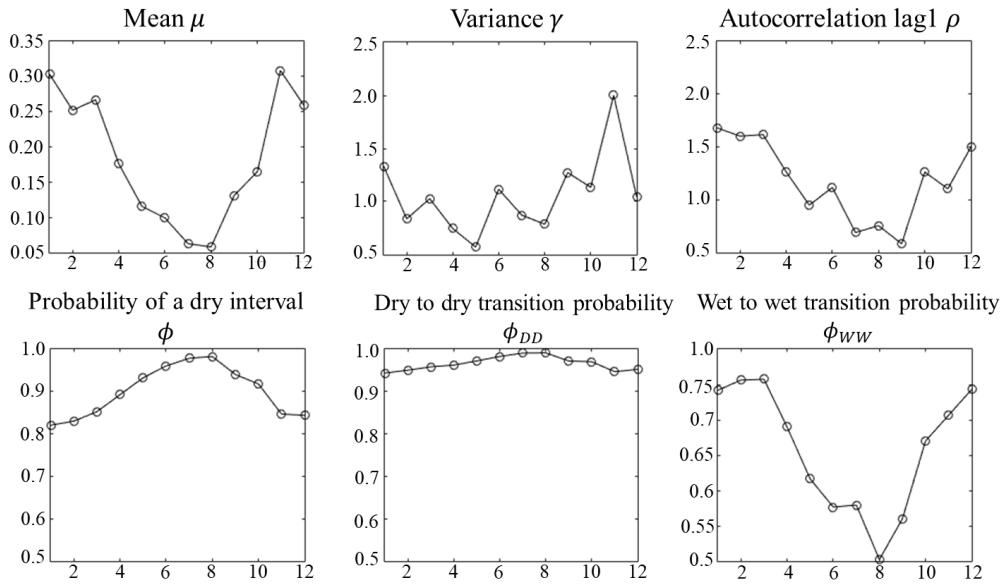


Figure A1. Monthly plot of hourly rainfall characteristics calculated based on the experimental data of the rain gauge of Cervinara.

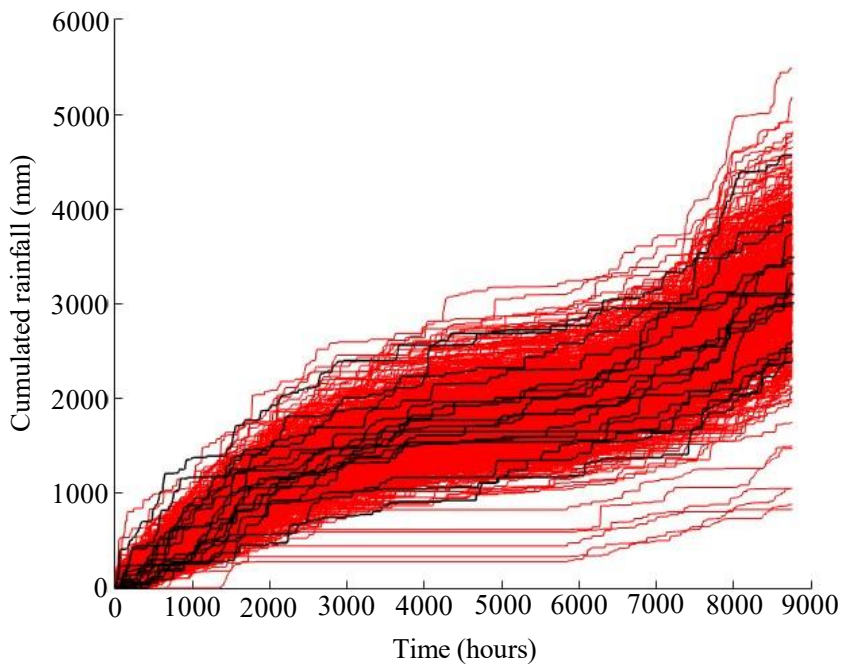
Table A1 gives the obtained parameters of the NSRP stochastic model, where λ represents the parameter of a Poisson process describing the arrival of clusters; ν is the mean number of cells in a cluster, also described by a Poisson process; β is the parameter of an exponential probability distribution describing the arrival times of each cell in a cluster, expressed as the number of time intervals of 10 minutes starting from the beginning of a cluster; η is the parameter of an exponential probability distribution describing the duration of rain cells; ξ is the parameter of a Weibull probability distribution describing the rain intensity of cells, with cumulative probability function $F(x, \xi, b) = 1 - \exp(-\xi x^b)$, in which x is cell rain intensity and the parameter $b = 0.8$ has been set a priori (Cowpertwait et al., 1996).

Table A1. Parameters of the NSRP model.

| <u>Param</u> | <u>Sept</u> | <u>Oct</u> | <u>Nov</u> | <u>Dec-</u> <u>Mar</u> | <u>Apr</u> | <u>May-</u> <u>Jun</u> | <u>Lug.</u> <u>Aug</u> |
|--------------|-------------|------------|------------|---------------------------|------------|---------------------------|---------------------------|
| : | | | | | | | |

| | | | | | | | |
|------------------------------|-------------|---------------|---------------|---------------|---------------|----------------|----------------|
| λ (h^{-1}) | <u>0.01</u> | <u>0.0052</u> | <u>0.0025</u> | | <u>0.0080</u> | | |
| | <u>5</u> | <u>4</u> | <u>7</u> | <u>0.0238</u> | <u>9</u> | <u>0.00386</u> | <u>0.00900</u> |
| ν (-) | <u>2.68</u> | <u>36.4</u> | <u>57.1</u> | <u>2.60</u> | <u>38.7</u> | <u>21.6</u> | <u>1.40</u> |
| β (h^{-1}) | <u>0.26</u> | | | | | | |
| | <u>5</u> | <u>0.156</u> | <u>0.0167</u> | <u>0.813</u> | <u>0.123</u> | <u>0.116</u> | <u>24.5</u> |
| η (h^{-1}) | <u>1.41</u> | <u>57.3</u> | <u>1.43</u> | <u>0.280</u> | <u>15.5</u> | <u>8.59</u> | <u>1.23</u> |
| ξ (h^b mm^{-b}) | <u>0.33</u> | | | | | | |
| | <u>0</u> | <u>0.047</u> | <u>0.450</u> | <u>0.967</u> | <u>0.186</u> | <u>0.158</u> | <u>0.268</u> |

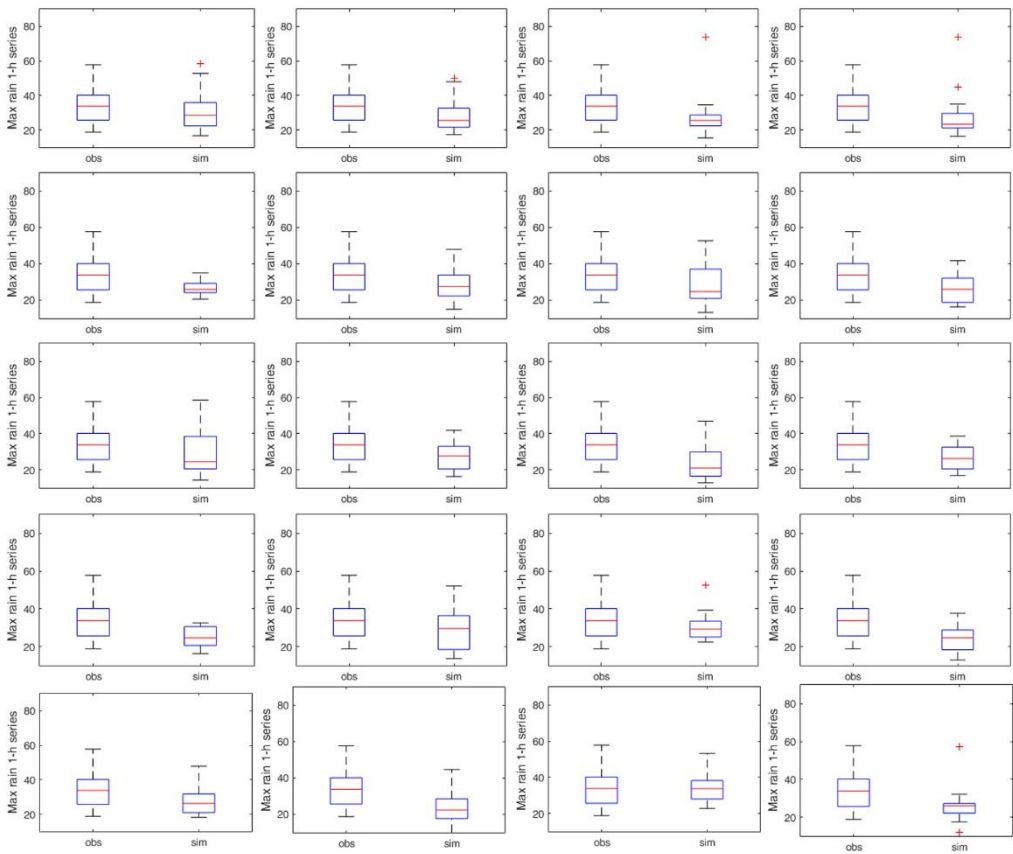
826 The adherence of the rainfall generated with the stochastic model to the
827 experimental rainfall data has been tested by evaluating rainfall characteristics
828 different from those used for the calibration. For instance, Figure A2 shows the
829 comparison of the rainfall depth, cumulated over one year, for the experimental
830 data (17 years) and for 1000 years of synthetic data generated with the calibrated
831 NSRP model.



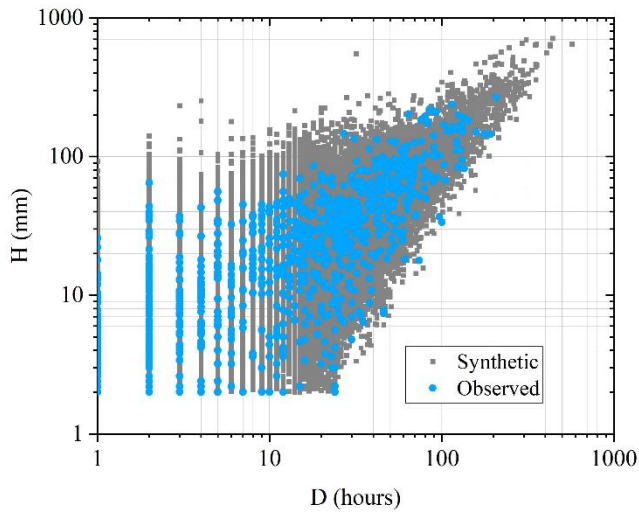
832

833 Figure A2. Comparison of observed (black) and simulated (red) cumulated rainfall
834 plots in a year.

835 In Figure A3, the boxplot of the maximum hourly rainfall in one year, observed
836 in the experimental dataset of 17 years, is compared with the same boxplot
837 referred to 20 series of 17 years randomly extracted from the generated 1000
838 years synthetic rainfall series. Several of the synthetic 17 years intervals show a
839 distribution of the maximum hourly rainfall close to the observed one.



840
841 Figure A3. Comparison of observed and simulated distributions (boxplots) of the
842 maximum hourly precipitation in a year, for series of the same length. Each panel
843 shows the distribution for the 17 observed years (boxplot is always the same), and
844 17 randomly picked simulated years.

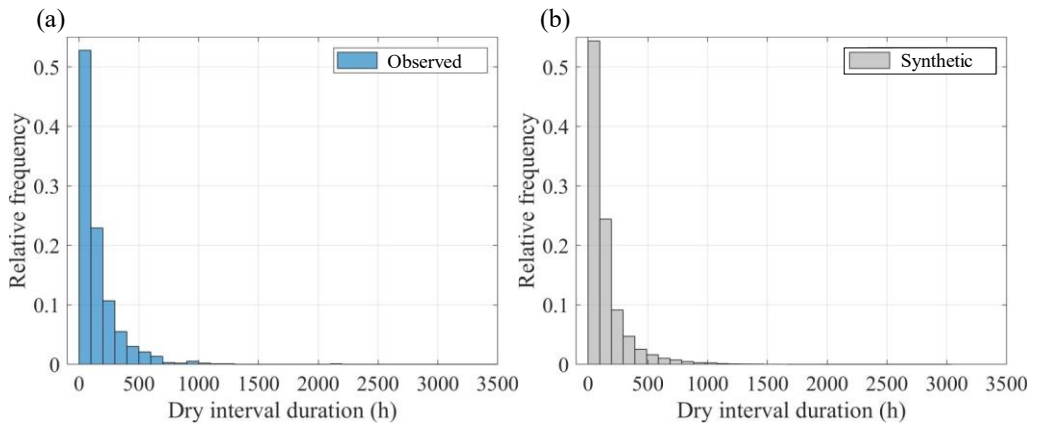


845

846 Figure A4. Scatterplot of total rainfall event depth (H) vs. rainfall event duration
 847 (D). The events have been sorted within the rainfall datasets by considering a
 848 separation “dry” interval of 24 hours with less than 2 mm rainfall. The blue dots
 849 represent events extracted from the 17 years experimental rainfall dataset, while
 850 the grey dots represent events extracted from the 1000 years synthetic rainfall
 851 dataset.

852 Regarding the required comparison between synthetic and observed wet and dry
 853 intervals, figure A4 shows the scatterplot of duration and total rain depth of the
 854 events, sorted with a separation “dry” interval of 24 hours with less than 2 mm
 855 rainfall from the observed dataset (blue dots) and the synthetic dataset (grey
 856 dots). The plots show how the synthetic data contain the observed ones, and that
 857 the shape of the dot clouds looks quite similar.

858 Figure A5 shows the frequency distributions of the durations of dry intervals
 859 belonging to the 17 years rainfall dataset, and the same distribution for the dry
 860 intervals extracted from the 1000 years synthetic dataset: the two distributions
 861 look nearly identical.



862
863 **Figure A5. Frequency distributions of dry interval durations for events extracted**
864 **from the 17 years experimental rainfall dataset (a) and events extracted from the**
865 **1000 years synthetic rainfall dataset (b). The events have been sorted within the**
866 **rainfall datasets by considering a separation “dry” interval of 24 hours with less**
867 **than 2 mm rainfall.**

869 **Appendix B: Tuning Random Forest hyperparameters**

870 The Random Forest (RF) algorithm (Breiman, 2001) has been very successful as
871 a general-purpose classification and regression method. Starting from Bagging
872 or Bootstrap Aggregation (Efron and Tibshirani, 1993), RF builds several random
873 de-correlated decision trees and then averages their predictions.

874 The regression RF algorithm can be summarized as follows: 1) by means of
875 bootstrap, a sample is extracted from the training data; 2) based on the
876 bootstrapped data, a tree T of the random-forest is grown by repeating the
877 following operations until a leaf node (a node without split) is reached: a) for
878 each node, m variables are randomly selected from the p input variables or
879 features (with $1 \leq m \leq p$); b) among the m variables, the best variable and
880 splitting point are selected according to a minimum criterium; c) the node is split
881 into two daughter nodes. To build the RF with B trees, steps 1 and 2 are repeated
882 B times. Then, the prediction, Y_{pred} , for a new observation, X , is the average of
883 the final values, $T_b(X)$, i.e., the values of the predicted variable corresponding to
884 the leaves of each tree:

885
$$Y_{pred} = \frac{1}{B} \sum_{b=1}^B T_b(X) \quad (B.1)$$

886 The main advantage of RF is the simplicity with which a forest can be trained,
887 and the parameters of the algorithms optimized. In this paper, the scikit-learn
888 framework (Pedregosa et al, 2011) is used to run the RF algorithm.

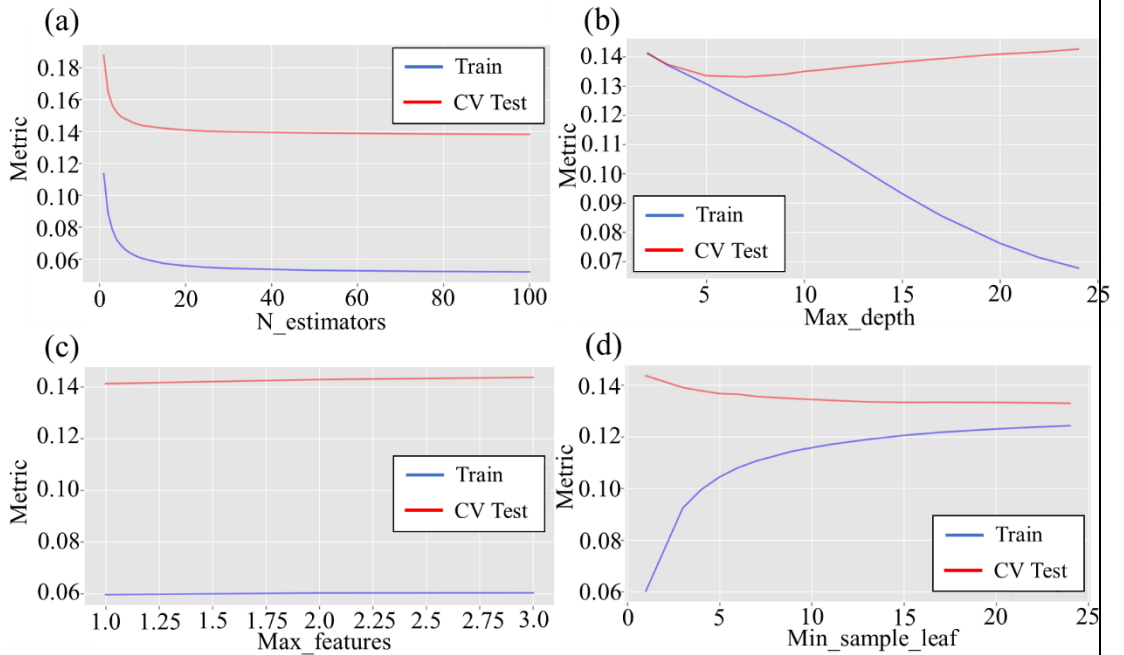
889 The main hyperparameters of a RF are: 1) `n_estimators`: the number of trees of
890 the forest; 2) `max_depth`: the maximum depth of each decision tree in the forest;
891 3) `min_samples_leaf`: the minimum number of samples required to be at a leaf
892 node; `max_features`: the number of features, or input variables, to consider when
893 looking for the best split.

894 The procedure applied in this study to estimate and optimize the hyperparameters
895 of the RF algorithm consists of the following steps:

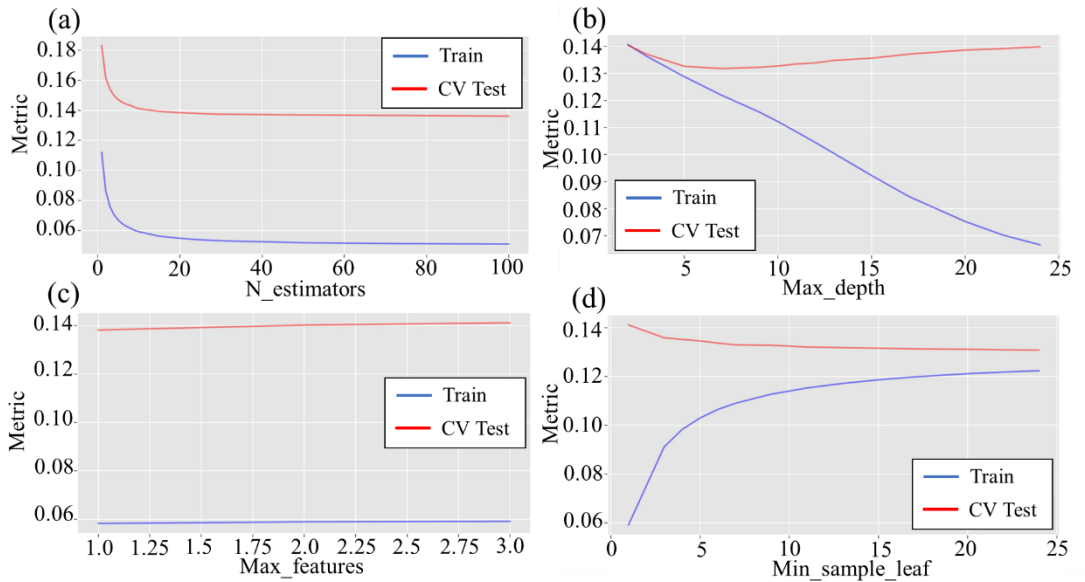
- 896 - Step 1: the dataset is divided into a training set and a test set, respectively
897 containing 80% and 20% of the data, randomly chosen.
- 898 - Step 2: the K-fold cross-validation technique (Stone, 1974), with K=10,
899 is applied to empirically determine a set of values for the
900 hyperparameters, using only the training dataset.
- 901 - Step 3: for each fold, a RF is trained on the other k-1 folds of the data and
902 tested on the first fold. This process is repeated k=10 times, so to use each of
903 the k folds exactly once as the validation set. A performance metric is then
904 calculated for each fold, to estimate how well the RF will perform on new
905 data. In this work the Root Mean Square Error (RMSE) is used as the
906 performance metric.
- 907 - Step 4: the RF is trained by changing one hyperparameters at once and using
908 the default values for the other three (default values of hyperparameters as
909 reported in Pedegrosa et al (2011) are: n_estimators=100; max_depth=none,
910 i.e., the tree is expanded until all leaves contain less samples than
911 min_samples_split; min_samples_leaf=1; max_features=1).
- 912 - Step 5: from the results of the previous step, the ranges of hyperparameters,
913 given in table B1, are defined. These values represent the grid in which the
914 optimal hyperparameters are searched. In other words, using the K-fold
915 technique (step 2), RF model is fitted K times, and then the optimal set of
916 values is the one minimizing the RMSE.
- 917 - Step 6 (validation of the model), once the optimal values of the
918 hyperparameters are determined, the performance of RF model is evaluated,
919 for the test dataset as defined in Step 1, using the RMSE.

920 In this study, the described methodology is used to evaluate the hyperparameters
921 for the following RF models: RF1, trained using the input features $\langle H, \theta_6, h_a \rangle$;

922 RF2, trained using $\langle H, \theta_{100}, h_a \rangle$; RF3, trained using $\langle H, \theta_6, \theta_{100} \rangle$; RF4, trained
 923 using $\langle H, \theta_6, \theta_{100} \rangle$. All models are trained to predict the normalized change of
 924 water storage in the soil mantle, $\Delta S/H$. Figures B1, B2, B3 and B4 show the
 925 results of step 4. Specifically, they depict the trends of the RMSE versus the
 926 hyperparameters for RF1, RF2, RF3 and RF4, respectively.



927
 928 **Figure B1. Performance of random forest model RF1 on the test and Cross**
 929 **Validation (CV) sets according to the test metric by changing the hyperparameters:**
 930 **(a) N_estimators (b) Max depth (c) Max features (d) Min samples leaf**



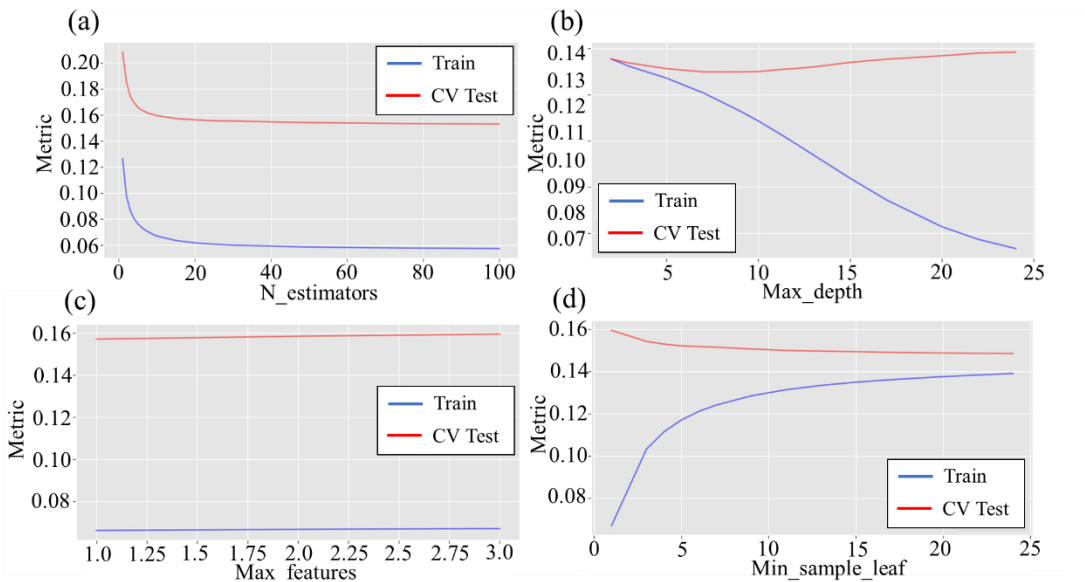
931

932

933

934

Figure B2. Performance of random forest model RF2 on the test and Cross Validation (CV) sets according to the test metric by changing the hyperparameters: (a) N_estimators (b) Max depth (c) Max features (d) Min samples leaf



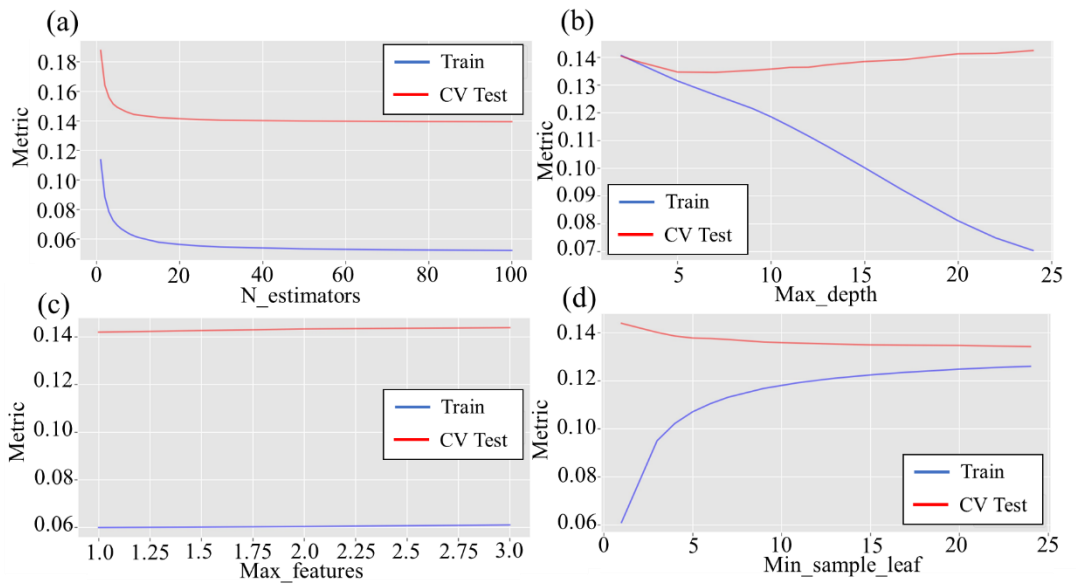
935

936

937

938

Figure B3. Performance of random forest model RF3 on the test and Cross Validation (CV) sets according to the test metric by changing the hyperparameters: (a) N_estimators (b) Max depth (c) Max features (d) Min samples leaf



939

940 **Figure B4. Performance of random forest model RF4 on the test and Cross**
 941 **Validation (CV) sets according to the test metric by changing the hyperparameters:**
 942 **(a) N_estimators (b) Max depth (c) Max features (d) Min samples leaf**

943 The analysis of the previous figures provides the search grid of hyperparameters
 944 given in Table B1. After fitting each model K times (step 5), the optimal sets of
 945 hyperparameters are reported in Table B2 for each RF model. Then, the
 946 performance of models RF1, RF2, RF3, and RF4 are evaluated on the test dataset
 947 using RMSE metric. The obtained results are summarized in Table B3.

948 The above-described analysis has been used to identify the most informative
 949 triplet of variables, which has been chosen as the one corresponding to the best
 950 performing among the optimal RF models, namely RF2.

951 **Table B1. Hyperparameters range of variation**

| <u>Hyperparameter</u> | <u>Range of variation</u> |
|------------------------------|----------------------------------|
| <u>n_estimators</u> | <u>5,10,20,25,30</u> |
| <u>max_features</u> | <u>1,2,3</u> |
| <u>min_samples leaf</u> | <u>15,20,25</u> |
| <u>max_depth</u> | <u>3,4, 5, 6,7</u> |

952

953 **Table B2. Optimal values of Hyperparameters**

| <u>Hyperparamete</u> | <u>Optimal values</u> | | | |
|-------------------------|-----------------------|------------|------------|------------|
| <u>r</u> | <u>RF1</u> | <u>RF2</u> | <u>RF3</u> | <u>RF4</u> |
| <u>n_estimators</u> | <u>30</u> | <u>30</u> | <u>25</u> | <u>30</u> |
| <u>max_features</u> | <u>2</u> | <u>2</u> | <u>3</u> | <u>2</u> |
| <u>min_samples_leaf</u> | <u>20</u> | <u>20</u> | <u>9</u> | <u>20</u> |
| <u>max_depth</u> | <u>7</u> | <u>7</u> | <u>7</u> | <u>7</u> |

954

955 **Table B3. RMSE of studied models computed for the test dataset**

| <u>Model</u> | <u>RMSE</u> |
|--|--------------|
| <u>RF1</u> $\langle H, \theta_6, h_a \rangle$ | <u>0.122</u> |
| <u>RF2</u> $\langle H, \theta_{100}, h_a \rangle$ | <u>0.120</u> |
| <u>RF3</u> $\langle H, \theta_6, \theta_{100} \rangle$ | <u>0.140</u> |
| <u>RF4</u> $\langle \theta_6, \theta_{100}, h_a \rangle$ | <u>0.124</u> |

956

957

958

959 **Author contributions**

960 RG and DR formulated the research aim; PM provided the field measurements;
961 PM and GS supplied the model simulations; DR and GS curated and analyzed
962 the data; RG oversighted the research activities; DR worked on the preparation
963 and the data visualization; DR, PM and GS wrote the draft manuscript; RG wrote
964 the final version of the manuscript.

965 **Acknowledgements**

966 This research is part of the Ph.D. project entitled “Hydrological controls and
967 geotechnical features affecting the triggering of shallow landslides in pyroclastic
968 soil deposits” within the Doctoral Course “A.D.I.” of Università degli Studi della
969 Campania “L. Vanvitelli”.

970 The research has been also funded by Università degli Studi della Campania ‘L.
971 Vanvitelli’ through the programme “VALERE: VAnviteLli pEr la RicErca”.

972 **References**

973 Allocca, V., Manna, F., and De Vita, P.: Estimating annual groundwater recharge
974 coefficient for karst aquifers of the southern Apennines (Italy), *Hydrol Earth Syst*
975 *Sci*, 18, 803–817, <https://doi.org/10.5194/hess-18-803-2014>, 2014.

976 Arthur, D. and Vassilvitskii, S.: k-means++: The Advantages of Careful Seeding,
977 in: *Proceedings of the Eighteenth Annual ACM-SIAM Symposium on Discrete*
978 *Algorithms*, 1027–1035, 2007.

979 Bogaard, T. A. and Greco, R.: Landslide hydrology: from hydrology to pore
980 pressure, *WIREs Water*, 3, 439–459, <https://doi.org/10.1002/wat2.1126>, 2016.

981 Bogaard, T. A. and Greco, R.: Invited perspectives: Hydrological perspectives on
982 precipitation intensity-duration thresholds for landslide initiation: proposing
983 hydro-meteorological thresholds, *Natural-Nat. Hazards-Haz. and Earth System*
984 *Sys. SciencesSci.*, 18, 31–39, <https://doi.org/10.5194/nhess-18-31-2018>, 2018.

- 985 ~~Bogaard, T. A. and Greco, R.: Landslide hydrology: from hydrology to pore~~
986 ~~pressure, Wiley Interdisciplinary Reviews: Water, 3, 439–459,~~
987 ~~<https://doi.org/10.1002/wat2.1126>, 2016a.~~
- 988 Bordoni, M., Meisina, C., Valentino, R., Lu, N., Bittelli, M., and Chersich, S.:
989 Hydrological factors affecting rainfall-induced shallow landslides: From the field
990 monitoring to a simplified slope stability analysis, *Eng. Geol.*,
991 <https://doi.org/10.1016/j.enggeo.2015.04.006>, 2015.
- 992 Breiman, L.: Random Forests, *Mach. Learn.*, 45, 5–32,
993 <https://doi.org/https://doi.org/10.1023/A:1010933404324>, 2001.
- 994 Capretti, P. and Battisti, A.: Water stress and insect defoliation promote the
995 colonization of *Quercus cerris* by the fungus *Biscogniauxia mediterranea*, *For.*
996 *Pathol.*, 37, 129–135, <https://doi.org/10.1111/J.1439-0329.2007.00489.X>, 2007.
- 997 Cascini, L., Cuomo, S., and Guida, D.: Typical source areas of May 1998 flow-
998 like mass movements in the Campania region, Southern Italy, *Eng. Geol.*, 96,
999 107–125, <https://doi.org/10.1016/j.enggeo.2007.10.003>, 2008.
- 1000 Cascini, L., Sorbino, G., Cuomo, S., and Ferlisi, S.: Seasonal effects of rainfall
1001 on the shallow pyroclastic deposits of the Campania region (southern Italy).
1002 *Landslides*, 11(5), 779–792. <https://doi.org/10.1007/s10346-013-0395-3>, 2014.
- 1003 Celico, F., Naclerio, G., Bucci, A., Nerone, V., Capuano, P., Carcione, M.,
1004 Allocca, V., and Celico, P.: Influence of pyroclastic soil on epikarst formation:
1005 A test study in southern Italy, *Terra Nova*, 22, 110–115,
1006 <https://doi.org/10.1111/J.1365-3121.2009.00923.X>, 2010.
- 1007 Chitu, Z., Bogaard, T. A., Busuioc, A., Burcea, S., Sandric, I., and Adler, M.-J.:
1008 *Identifying hydrological pre-conditions and rainfall triggers of slope failures at*
1009 *catchment scale for 2014 storm events in the Ialomita Subcarpathians, Romania,*
1010 *Landslides*, 14, 419–434, <https://doi.org/10.1007/s10346-016-0740-4>, 2017.

1011 Comegna, L., Damiano, E., Greco, R., Guida, A., Olivares, L., and Picarelli, L.:
1012 Field hydrological monitoring of a sloping shallow pyroclastic deposit, Canadian
1013 Can. Geotechnical—Geotech. Journal, 53, 1125–1137,
1014 <https://doi.org/10.1139/cgj-2015-0344>, 2016.

1015 Cowpertwait, P. S. P., O’Connell, P. E., Metcalfe, A. V., and Mawdsley, J. A.:
1016 Stochastic point process modelling of rainfall. I. Single-site fitting and validation,
1017 J. Hydrol. (Amst), [https://doi.org/10.1016/S0022-1694\(96\)80004-7](https://doi.org/10.1016/S0022-1694(96)80004-7), 1996.

1018 Dal Soglio, L., Danquigny, C., Mazzilli, N., Emblanch, C., and Massonnat, G.:
1019 Taking into Account both Explicit Conduits and the Unsaturated Zone in Karst
1020 Reservoir Hybrid Models: Impact on the Outlet Hydrograph. Water, 12, 3221,
1021 <https://doi.org/10.3390/w12113221>, 2020.

1022 Damiano, E. and Olivares, L.: The role of infiltration processes in steep slope
1023 stability of pyroclastic granular soils: laboratory and numerical investigation,
1024 Natural Nat. Hazards Haz., 52, 329–350, [https://doi.org/10.1007/s11069-009-](https://doi.org/10.1007/s11069-009-9374-3)
1025 [9374-3](https://doi.org/10.1007/s11069-009-9374-3), 2010.

1026 Damiano, E., Olivares, L., and Picarelli, L.: Steep-slope monitoring in
1027 unsaturated pyroclastic soils, Eng. Geol., 137–138, 1–12,
1028 <https://doi.org/10.1016/j.enggeo.2012.03.002>, 2012.

1029 Damiano, E., Greco, R., Guida, A., Olivares, L., and Picarelli, L.: Investigation
1030 on rainwater infiltration into layered shallow covers in pyroclastic soils and its
1031 effect on slope stability, Eng. Geol., 220, 208–218,
1032 <https://doi.org/10.1016/j.enggeo.2017.02.006>, 2017.

1033 de Amorim, R. C. and Hennig, C.: Recovering the number of clusters in data sets
1034 with noise features using feature rescaling factors, Inf. Sci. (N Y), 324, 126–145,
1035 <https://doi.org/10.1016/J.INS.2015.06.039>, 2015.

1036 De Vita, P., Agrello, D., and Ambrosino, F.: Landslide susceptibility assessment
1037 in ash-fall pyroclastic deposits surrounding Mount Somma-Vesuvius:
1038 Application of geophysical surveys for soil thickness mapping, *J. Appl.*
1039 *Geophys.*, 59, 126–139, <https://doi.org/10.1016/j.jappgeo.2005.09.001>, 2006.

1040 [Efron, B. and Tibshirani, R.J., An Introduction to the Bootstrap. Chapman and](#)
1041 [Hall, New York. https://doi.org/10.1007/978-1-4899-4541-9, 1993.](#)

1042 Feddes, R. A., Kowalik, P., Kolinska-Malinka, K., and Zaradny, H.: Simulation
1043 of field water uptake by plants using a soil water dependent root extraction
1044 function, *J. Hydrol.—(Amst)*, 31, 13–26, [https://doi.org/10.1016/0022-](https://doi.org/10.1016/0022-1694(76)90017-2)
1045 [1694\(76\)90017-2](https://doi.org/10.1016/0022-1694(76)90017-2), 1976.

1046 Fiorillo, F., Guadagno, F., Aquino, S., and De Blasio, A.: The December 1999
1047 Cervinara landslides: Further debris flows in the pyroclastic deposits of
1048 Campania (Southern Italy), ~~*Bulletin*~~ [Bull. of Engineering Eng. Geology Geol.](#)
1049 [and the Environment Env.](#), <https://doi.org/10.1007/s100640000093>, 2001.

1050 [Forestieri, A., Caracciolo, D., Arnone, E., and Noto, L.V.: Derivation of Rainfall](#)
1051 [Thresholds for Flash Flood Warning in a Sicilian Basin Using a Hydrological](#)
1052 [Model, Procedia Engineering, 154, 818-825, ISSN 1877-7058,](#)
1053 <https://doi.org/10.1016/j.proeng.2016.07.413>, 2016.

1054 Gao, S. and Shain, L.: Effects of water stress on chestnut blight, ~~*Canadian*~~ [Can.](#)
1055 [journal J. of forest For. research Res.](#), 25, 1030–1035, 1995.

1056 Greco, R. and Gargano, R.: A novel equation for determining the suction stress
1057 of unsaturated soils from the water retention curve based on wetted surface area
1058 in pores, *Water Resour Res*, 51, 6143–6155,
1059 <https://doi.org/10.1002/2014WR016541>, 2015.

1060 Greco, R., Comegna, L., Damiano, E., Guida, A., Olivares, L., and Picarelli, L.:
1061 Hydrological modelling of a slope covered with shallow pyroclastic deposits

1062 from field monitoring data, *Hydrol. Earth Syst. Sci.*, 17, 4001–4013,
1063 <https://doi.org/10.5194/hess-17-4001-2013>, 2013.

1064 Greco, R., Comegna, L., Damiano, E., Guida, A., Olivares, L., and Picarelli, L.:
1065 Conceptual Hydrological Modeling of the Soil-bedrock Interface at the Bottom
1066 of the Pyroclastic Cover of Cervinara (Italy), *Procedia Earth and Planetary*
1067 *Science*, <https://doi.org/10.1016/j.proeps.2014.06.007>, 2014.

1068 Greco, R., Marino, P., Santonastaso, G. F., and Damiano, E.: Interaction between
1069 Perched Epikarst Aquifer and Unsaturated Soil Cover in the Initiation of Shallow
1070 Landslides in Pyroclastic Soils, *Water—(Basel)*, 10, 948,
1071 <https://doi.org/10.3390/w10070948>, 2018.

1072 Greco, R., Comegna, L., Damiano, E., Marino, P., Olivares, L., and Santonastaso,
1073 G. F.: Recurrent rainfall-induced landslides on the slopes with pyroclastic cover
1074 of Partenio Mountains (Campania, Italy): Comparison of 1999 and 2019 events,
1075 *Eng Geol*, 288, 106160, <https://doi.org/10.1016/j.enggeo.2021.106160>, 2021.

1076 [Greco, R., Marino, P., and Bogaard, T. A.: Recent Advancements of Landslide](#)
1077 [Hydrology, *WIREs Water*, e1675. <https://doi.org/10.1002/wat2.1675>, 2023.](#)

1078 Hartmann, A., Goldscheider, N., Wagener, T., Lange, J., and Weiler, M.: Karst
1079 water resources in a changing world: Review of hydrological modeling
1080 approaches, *Reviews of Geophysics*, 52, 218–242,
1081 <https://doi.org/10.1002/2013RG000443>, 2014.

1082 Hastie, T., Tibshirani, R., and Friedman, J.: *The Elements of Statistical Learning*
1083 *Data Mining, Inference, and Prediction*, 2nd ed., Springer Series on Statistics,
1084 Stanford, 1–763 pp., 2008.

1085 Lloyd, S. P.: Least Squares Quantization in PCM, *IEEE Trans. Inf. Theory*, 28,
1086 1982.

1087 Lu, N. and Likos, W. J.: Suction Stress Characteristic Curve for Unsaturated Soil,
1088 ~~Journal of Geotechnical and Geoenvironmental Engineering~~,
1089 [https://doi.org/10.1061/\(asce\)1090-0241\(2006\)132:2\(131\)](https://doi.org/10.1061/(asce)1090-0241(2006)132:2(131)), 2006.

1090 Marino, P., Comegna, L., Damiano, E., Olivares, L., and Greco, R.: Monitoring
1091 the Hydrological Balance of a Landslide-Prone Slope Covered by Pyroclastic
1092 Deposits over Limestone Fractured Bedrock, ~~Water (Basel)~~, 12, 3309,
1093 <https://doi.org/10.3390/w12123309>, 2020a.

1094 ~~Marino, P., Peres, D.J., Cancelliere, A., Greco, R. and Bogaard, T. A.: Soil~~
1095 ~~moisture information can improve shallow landslide forecasting using the~~
1096 ~~hydrometeorological threshold approach, Landslides 17, 2041–2054,~~
1097 ~~<https://doi.org/10.1007/s10346-020-01420-8>, 2020b.~~

1098 Marino, P., Santonastaso, G. F., Fan, X., and Greco, R.: Prediction of shallow
1099 landslides in pyroclastic-covered slopes by coupled modeling of unsaturated and
1100 saturated groundwater flow, *Landslides*, [https://doi.org/10.1007/s10346-020-](https://doi.org/10.1007/s10346-020-01484-6)
1101 [01484-6](https://doi.org/10.1007/s10346-020-01484-6), 2021**0b**.

1102 McDowell, N., Pockman, W. T., Allen, C. D., Breshears, D. D., Cobb, N., Kolb,
1103 T., Plaut, J., Sperry, J., West, A., Williams, D. G., and Yezpez, E. A.: Mechanisms
1104 of plant survival and mortality during drought: Why do some plants survive while
1105 others succumb to drought?, *New Phytologist*, 178, 719–739,
1106 <https://doi.org/10.1111/J.1469-8137.2008.02436.X>, 2008.

1107 ~~Neyman, J. and Scott, E. L.: Statistical Approach to Problems of Cosmology,~~
1108 ~~Journal of the Royal Statistical Society: Series B (Methodological),~~
1109 ~~<https://doi.org/10.1111/j.2517-6161.1958.tb00272.x>, 1958.~~

1110 Nieber, J. L. and Sidle, R. C.: How do disconnected macropores in sloping soils
1111 facilitate preferential flow?, *Hydrological Processes*, 24, 1582–1594,
1112 <https://doi.org/10.1002/hyp.7633>, 2010.

1113 Olivares, L. and Picarelli, L.: Shallow flowslides triggered by intense rainfalls on
1114 natural slopes covered by loose unsaturated pyroclastic soils, *Geotechnique*,
1115 <https://doi.org/10.1680/geot.2003.53.2.283>, 2003.

1116 Pagano, L., Picarelli, L., Rianna, G., and Urciuoli, G.: A simple numerical
1117 procedure for timely prediction of precipitation-induced landslides in unsaturated
1118 pyroclastic soils, *Landslides*, 7, 273–289, [https://doi.org/10.1007/s10346-010-](https://doi.org/10.1007/s10346-010-0216-x)
1119 [0216-x](https://doi.org/10.1007/s10346-010-0216-x), 2010.

1120 Pan, S., Pan, N., Tian, H., Friedlingstein, P., Sitch, S., Shi, H., Arora, V. K.,
1121 Haverd, V., Jain, A. K., Kato, E., Lienert, S., Lombardozzi, D., Nabel, J. E. M.
1122 S., Ottlé, C., Poulter, B., Zaehle, S., and Running, S. W.: Evaluation of global
1123 terrestrial evapotranspiration using state-of-the-art approaches in remote sensing,
1124 machine learning and land surface modeling, *Hydrol. Earth Syst. Sci.*, 24, 1485–
1125 1509, <https://doi.org/10.5194/hess-24-1485-2020>, 2020.

1126 Paulik, C., Dorigo, W., Wagner, W., and Kidd, R.: Validation of the ASCAT Soil
1127 Water Index using in situ data from the International Soil Moisture Network,
1128 ~~*International Int. Journal J. of Applied Appl. Earth Obs. ervation and*~~
1129 ~~*Geoinformation Geoinf.*~~, 30, 1–8, <https://doi.org/10.1016/J.JAG.2014.01.007>,
1130 2014.

1131 ~~*Pedregosa, F., Varoquaux, G., Gramfort, A., Michel, V., Thirion, B., Grisel, O.,*~~
1132 ~~*Blondel, M. Prettenhofer, P., Weiss, R., Dubourg, V., Vanderplas, J., Passos, A.,*~~
1133 ~~*Cournapeau, D., Brucher, M., Perrot, M., and Duchesnay, E.: Scikit-learn:*~~
1134 ~~*Machine Learning in Python. J. Mach. Lear. Res., 12, 2825–2830, 2011.*~~

1135 Peres, D. J. and Cancelliere, A.: Derivation and evaluation of landslide-triggering
1136 thresholds by a Monte Carlo approach, *Hydrol. Earth Syst. Sci.*, 18, 4913–4931,
1137 <https://doi.org/10.5194/hess-18-4913-2014>, 2014.

- 1138 [Peres, D. J., Cancelliere, A., Greco, R., and Bogaard, T. A.: Influence of uncertain](#)
1139 [identification of triggering rainfall on the assessment of landslide early warning](#)
1140 [thresholds, Nat. Hazards Earth. Syst. Sci., 18, 633–646,](#)
1141 <https://doi.org/10.5194/nhess-18-633-2018>, 2018.
- 1142 [Perrin, J., Jeannin, P. Y., and Zwahlen, F.: Epikarst storage in a karst aquifer: A](#)
1143 [conceptual model based on isotopic data, Milandre test site, Switzerland. J.](#)
1144 [Hydrol., 279\(1-4\), 106-124, https://doi.org/10.1016/S0022-1694\(03\)00171-9,](#)
1145 [2003.](#)
- 1146 Pirone, M., Papa, R., Nicotera, M. V., and Urciuoli, G.: Soil water balance in an
1147 unsaturated pyroclastic slope for evaluation of soil hydraulic behaviour and
1148 boundary conditions, *J. Hydrol. (Amst)*,
1149 <https://doi.org/10.1016/j.jhydrol.2015.06.005>, 2015.
- 1150 Ponce, V. M. and Hawkins, R. H.: Runoff Curve Number: Has It Reached
1151 Maturity?, *J. Hydrol. Eng.*, 1, 11–19, [https://doi.org/10.1061/\(ASCE\)1084-](https://doi.org/10.1061/(ASCE)1084-)
1152 [0699\(1996\)1:1\(11\)](https://doi.org/10.1061/(ASCE)1084-0699(1996)1:1(11)), 1996.
- 1153 Revellino, P., Guerriero, L., Gerardo, G., Hungr, O., Fiorillo, F., Esposito, L.,
1154 and Guadagno, F. M.: Initiation and propagation of the 2005 debris avalanche at
1155 Nocera Inferiore (Southern Italy), ~~Italian-Ital. Journal of. Geosciences~~*Geosci.*,
1156 <https://doi.org/10.3301/IJG.2013.02>, 2013.
- 1157 [Reichenbach, P., Cardinali, M., De Vita, P., and Guzzetti, F.: Regional](#)
1158 [hydrological thresholds for landslides and floods in the Tiber River Basin \(central](#)
1159 [Italy\), Environ. Geol., 35, 146–159, https://doi.org/10.1007/s002540050301,](#)
1160 [1998.](#)
- 1161 Richards, L. A.: Capillary conduction of liquids through porous mediums, *J.*
1162 *Appl. Phys.*, <https://doi.org/10.1063/1.1745010>, 1931.

1163 Rodriguez-Iturbe, I., Febres De Power, B., and Valdes, J. B.: Rectangular pulses
1164 point process models for rainfall: analysis of empirical data, *J. Geophys. Res.*,
1165 <https://doi.org/10.1029/JD092iD08p09645>, 1987.

1166 Rolandi, G., Bellucci, F., Heizler, M. T., Belkin, H. E., and De Vivo, B.: Tectonic
1167 controls on the genesis of ignimbrites from the Campanian Volcanic Zone,
1168 southern Italy, *Mineral-Miner. Petrol.*, 79, 3–31, [https://doi.org/10.1007/s00710-](https://doi.org/10.1007/s00710-003-0014-4)
1169 [003-0014-4](https://doi.org/10.1007/s00710-003-0014-4), 2003.

1170 Rousseeuw, P. J.: Silhouettes: A graphical aid to the interpretation and validation
1171 of cluster analysis, *J. Comput. Appl. Math.*, 20, 53–65,
1172 [https://doi.org/10.1016/0377-0427\(87\)90125-7](https://doi.org/10.1016/0377-0427(87)90125-7), 1987.

1173 [Segoni, S., Piciullo, L. and Gariano, S.L.: A review of the recent literature on](https://doi.org/10.1007/s10346-018-0966-4)
1174 [rainfall thresholds for landslide occurrence, *Landslides*, 15, 1483–1501,](https://doi.org/10.1007/s10346-018-0966-4)
1175 <https://doi.org/10.1007/s10346-018-0966-4>, 2018.

1176 Shuttleworth, W. J.: Evaporation, in: Handbook of Hydrology, edited by:
1177 Maidment, D. R., McGraw-Hill, New York, NY, USA, 1993.

1178 [Stone M.: Cross-validators choice and assessment of statistical predictions. *J.*](https://doi.org/10.2307/2343333)
1179 [*Royal Stat. Soc.*, 36\(2\), 111–147, 1974.](https://doi.org/10.2307/2343333)

1180 Tromp-Van Meerveld, H. J. and McDonnell, J. J.: Threshold relations in
1181 subsurface stormflow: 1. A 147-storm analysis of the Panola hillslope, *Water*
1182 *Resour. Res.*, 42, 2410, <https://doi.org/10.1029/2004WR003778>, 2006a.

1183 Tromp-Van Meerveld, H. J. and McDonnell, J. J.: Threshold relations in
1184 subsurface stormflow: 2. The fill and spill hypothesis, *Water Resour. Res.*,
1185 <https://doi.org/10.1029/2004WR003800>, 2006b.

1186 Tufano, R., Formetta, G., Calcaterra, D., and De Vita, P.: Hydrological control
1187 of soil thickness spatial variability on the initiation of rainfall-induced shallow

1188 landslides using a three-dimensional model, *Landslides*, 18, 3367-3380,
1189 <https://doi.org/10.1007/s10346-021-01681-x>, 2021.

1190 Twarakavi, N. K. C., Sakai, M., and Šimůnek, J.: An objective analysis of the
1191 dynamic nature of field capacity, *Water Resour. Res.*, 45,
1192 <https://doi.org/10.1029/2009WR007944>, 2009.

1193 van Genuchten, M. Th.: A Closed-form Equation for Predicting the Hydraulic
1194 Conductivity of Unsaturated Soils1, *Soil Science-Soci. of America-Am.*
1195 *Journal*, 44, 892, <https://doi.org/10.2136/sssaj1980.03615995004400050002x>,
1196 1980.

1197 Wicki, A., Lehmann, P., Hauck, C., Seneviratne, S. I., Waldner, P., and Stähli,
1198 M.: Assessing the potential of soil moisture measurements for regional landslide
1199 early warning, *Landslides*, 17, 1881–1896, [https://doi.org/10.1007/S10346-020-](https://doi.org/10.1007/S10346-020-01400-Y)
1200 [01400-Y](https://doi.org/10.1007/S10346-020-01400-Y)/**FIGURES/11**, 2020.

1201 Williams, P. W.: The role of the epikarst in karst and cave hydrogeology: a
1202 review, *Int. J. Speleol.*, 37, 1–10, <https://doi.org/10.5038/1827-806X.37.1.1>,
1203 2008.

1204